ARTICLE IN PRESS

Communications Biology

https://doi.org/10.1038/s42003-026-09866-7

Article in Press

Transcriptional and functional profiles of muscarinic receptor-expressing neurons in primate lateral prefrontal and anterior cingulate cortices

Received: 12 June 2025

Accepted: 4 March 2026

Cite this article as: Tsolias, A., Mojica, C.A., Yamani, R. *et al.* Transcriptional and functional profiles of muscarinic receptor-expressing neurons in primate lateral prefrontal and anterior cingulate cortices. *Commun Biol* (2026). https://doi.org/10.1038/s42003-026-09866-7

Alexandra Tsolias, Chromewell A. Mojica, Raghad Yamani, Sonal D. Khanna, Salam Al Abdullatif, Benjamin J. Snyder, Wayne Chang, Teresa Guillamon-Vivancos, Joseph Goodliffe, Angela L. Capriglione, Yuxin Zhou, Isabel Luisa Tan Palanca, Joaquin Martinez, Joshua D. Campbell, Jennifer I. Luebke, Ella Zeldich & Maria Medalla

We are providing an unedited version of this manuscript to give early access to its findings. Before final publication, the manuscript will undergo further editing. Please note there may be errors present which affect the content, and all legal disclaimers apply.

If this paper is publishing under a Transparent Peer Review model then Peer Review reports will publish with the final article.

ARTICLE IN PRESS

© The Author(s) 2026. **Open Access** This article is licensed under a Creative Commons Attribution-NonCommercial-NoDerivatives 4.0 International License, which permits any non-commercial use, sharing, distribution and reproduction in any medium or format, as long as you give appropriate credit to the original author(s) and the source, provide a link to the Creative Commons licence, and indicate if you modified the licensed material. You do not have permission under this licence to share adapted material derived from this article or parts of it. The images or other third party material in this article are included in the article's Creative Commons licence, unless indicated otherwise in a credit line to the material. If material is not included in the article's Creative Commons licence and your intended use is not permitted by statutory regulation or exceeds the permitted use, you will need to obtain permission directly from the copyright holder. To view a copy of this licence, visit http://creativecommons.org/licenses/by-nc-nd/4.0/.

Title: Transcriptional and functional profiles of muscarinic receptor-expressing neurons in primate lateral prefrontal and anterior cingulate cortices

Author names and affiliations, including postal codes:

Alexandra Tsolias[1#], Chromewell A. Mojica[1#], Raghad Yamani[1,5], Sonal D. Khanna[1], Salam Al Abdullatif[2], Benjamin J. Snyder[1], Wayne Chang[1], Teresa Guillamon-Vivancos[1,6], Joseph Goodliffe[1], Angela L. Capriglione[1], Yuxin Zhou[1], Isabel Luisa Tan Palanca[1], Joaquin Martinez[1], Joshua D. Campbell[2], Jennifer I. Luebke[1,3,4*], Ella Zeldich[1,3,4*] and Maria Medalla[1,3, 4*]

1. Department of Anatomy & Neurobiology, Boston University Chobanian & Avedisian School of Medicine, Boston, MA, USA
2. Department of Medicine, Boston University Chobanian & Avedisian School of Medicine, Boston MA, USA
3. Center for Systems Neuroscience, Boston University, Boston, MA, USA
4. Neurophotonics Center, Boston University, Boston, MA, USA
5. Department of Biochemistry, Faculty of Science, King AbdulAziz University, Jeddah. Saudi Arabia
6. Centro de Neurociencias Cajal-CSIC, Avenida de León, 1 28805, Madrid, Spain

[#] These authors contributed equally
*These authors jointly supervised this work

Corresponding author email address: mmedalla@bu.edu

Conflict of Interest Statement: All authors declare that they have no conflicts of interest.

Acknowledgments:
We thank Drs. Douglas Rosene and Tara Moore for access to resources and providing tissue for the experiments; Bethany Bowley, Samantha Calderazzo, Alexander Hsu, Eli Shobin, Penny Shultz Ajay Uprety, Katelyn Batterman, Karen Bottenfield, Karen Slater, and Veronica Go for technical assistance during perfusion and brain cutting. We also thank Dr. Yuriy Alekseyev and the members of the Boston University Chobanian & Avedisian School of Medicine Microarray and Sequencing Resource Core and Flow Cytometry Core for their help and guidance with the sequencing experiments.

We are grateful to NIH agencies for their support: NIH/NIMH R21MH126250 (MPI: M. Medalla and E. Zeldich), NIH/NIA R21AG072069 (MPIs: J. I. Luebke and E Zeldich), NIH/NIMH R01 MH116008 (PI: M. Medalla); NIH/NIA: R01-AG059028 (MPIs: J. I. Luebke and P. Hof), R01LM013154 (PI: J.D.C), R01/RF1AG068168 (PI: TL Moore) and RF1-AG043640 (PI: D. L. Rosene).

ARTICLE IN PRESS

Author contributions:
AT, CAM and MM designed and performed aspects of all the experiments and aided in the bioinformatics analysis, interpreted the results, and wrote the first drafts of the paper. MM, EZ, and JL conceived and oversaw the project, designed and performed aspects of all experiments and analyses, provided guidance, interpreted the results, and wrote the paper. SDK, RY, SA, and JDC designed and performed bioinformatics and statistical analyses for snRNA-seq dataset and edited the paper. BJS, WC, TGV, JG, AC, YZ, ILT, and JM helped perform experiments, gather and analyze data, and edited the manuscript.

Data availability:
Raw and processed snRNA-seq data generated in this study have been deposited in the NCBI Gene Expression Omnibus database (GEO accession # GSE296153). Source data are provided in the Source Data files in Supplementary Materials.

Code availability:
The R scripts used for data analysis are available on GitHub [https://github.com/campbio-manuscripts/Muscarinic_snRNAseq_ePhys].

Competing interests: The authors declare no competing interests.

Abstract:
Acetylcholine differentially modulates anterior cingulate (ACC) and lateral prefrontal (LPFC) cortices for cognitive-emotional integration, but cell-specific expression and function of muscarinic receptors (mAChR) and corresponding *CHRM1-4* genes in these areas of the primate brain are largely unknown. Our single-nucleus RNA sequencing and mRNA-protein histology in macaques revealed *CHRM3* as the most enriched mAChR gene in neurons, while m1 predominates at the protein level, likely due to nuclear retention of *CHRM3* and cytoplasmic trafficking of *CHRM1*. *CHRM3* and *CHRM1* showed strong co-expression and functional overlap, and were transcriptomically-distinct from *CHRM2,* which was uniquely enriched in deep layer excitatory and *PVALB*+ inhibitory neurons. Between-region comparisons showed that *CHRM3* is enriched in LPFC relative to ACC excitatory neurons. Further, *CHRM1-3*+ neurons showed region-specific transcriptomic signatures, with upregulation of synaptic plasticity genes in ACC relative to LPFC. Functional *in vitro* experiments confirmed a robust cholinergic-mediated decrease in excitatory and increase in inhibitory synaptic tone specific to ACC neurons, accompanied by changes in spine morphology. In contrast, cholinergic stimulation reduced inhibitory current amplitude in LPFC, shifting the microcircuit towards a stronger excitatory tone. These findings highlight region-specific acetylcholine signaling essential for flexible processing, learning and memory, which may underlie neurochemical circuit imbalance in neuropsychiatric disorders.

ARTICLE IN PRESS

ARTICLE IN PRESS

Introduction

The lateral prefrontal cortex (LPFC) and the anterior cingulate cortex (ACC) are two key regions of the frontal executive control network, essential for higher-order cognitive functions [reviewed in[1,2]]. Acetylcholine (ACh) is a robust neuromodulator of excitatory and inhibitory circuit dynamics and plasticity within these higher-order areas, mediating learning, memory and flexible behavior [[3-7]; reviewed in[8-11]]. The ACC, as part of the limbic system, receives markedly denser cholinergic projections compared to the LPFC[12,13]. The ACC communicates with limbic centers for arousal and emotions and sends contextual and motivational information to LPFC to guide behavior[14-24]. In rodent limbic medial temporal lobe structures [reviewed[25]], ACh enables switching across arousal states and oscillatory dynamics to mediate selective gating of inputs for motivational and mnemonic processing[4,26]. Similar mechanisms may be at play within ACC- LPFC networks that integrate cognitive-motivational information across diverse timescales [[24,27-32]; reviewed in[11,33]]. However, effects of cholinergic modulation on distinct cell types in these diverse higher-order frontal areas are largely unknown in primates.

ARTICLE IN PRESS

Diverse cortical cholinergic modulation is predominantly mediated by metabotropic G-protein coupled muscarinic receptor (mAChR) m1-m4 subtypes of two broad pharmacological classes, associated with distinct downstream signaling pathways [[34]; reviewed in[9,10]]. The M1/M3 class includes postsynaptically localized m1 and m3 subtypes coupled to $G_{q/11}$ proteins, which promote activation of protein kinase C (PKC) and downstream neuronal excitation [[34,35] reviewed in[10,36]]. Conversely, the M2/M4 class includes presynaptic m2 and m4 subtypes coupled to $G_{i/o}$ proteins, which inhibit the function of adenylyl cyclase and reduce cAMP[9,10]. Activation of M2/M4 receptors alters the activity of potassium (K^+) channels and calcium (Ca^{2+}) channels, resulting in the suppression of neurotransmitter release[34,37,38].

ARTICLE IN PRESS

The binding of ACh to different mAChRs can result in diverse excitatory or inhibitory effects depending upon the initiation of specific signaling cascades[39]. In previous studies[40,41], we found that the laminar distribution and subcellular structural localization of m1 and m2 mAChR proteins are distinct across frontal areas and neuronal subclasses. The current study aims to identify transcriptional regulation associated with mAChR m1-4 subtype gene (*CHRM1-4*) expression in ACC and LPFC excitatory (ExNs) and inhibitory neurons (InNs), using single-nucleus RNA sequencing (snRNA-seq), and to assess the functional effects of cholinergic activation on excitatory and inhibitory synapses using the cholinergic agonist, carbachol (CCH), during *in vitro* whole-cell patch-clamp electrophysiological recordings in adult rhesus monkeys. Our findings pave the way to understanding how region- and cell- specific cholinergic modulation may differentially affect distinct cognitive domains and learning and memory functions that are disrupted in cognitive and affective disorders.

ARTICLE IN PRESS

Results

Cell-specific mAChR subtype gene expression patterns across ACC and LPFC: predominant enrichment of CHRM3+

To assess cell-type specific transcriptional profiles associated with mAChR enrichment, we isolated 9,195 nuclei from the ACC area 24 and 8,147 nuclei from the LPFC area 46 of adult rhesus monkeys for snRNA-seq (Fig. 1A, B, Supplementary Fig. 1A-D; from n = 4 monkeys; Supplementary Table 1). Analyses identified clusters corresponding to 7 major cell types based on expression of canonical cell-specific markers: ExN, InN, microglia, astrocytes (Astr), oligodendrocytes (OL), oligodendrocyte precursor cells (OPCs) and "other" cells (mainly pericytes and endocytes)[42-46] (Fig. 1B, Supplementary Fig. 1E-K; and Supplementary Table 2).

ARTICLE IN PRESS

Distinct neuronal and glial cell clusters expressed *CHRM1-4* genes (Fig. 1C, D), in proportions remarkably similar between ACC and LPFC (Fig. 1E, F). Unexpectedly, while m1 and m2 mAChRs predominate at the protein level in the cortex[47], our findings revealed *CHRM3* (m3) to be the most widely expressed mAChR mRNA in both ACC and LPFC, detected in ~51-55% of all cells (Fig. 1C-E). Only about ~7% and ~10% of all cells expressed *CHRM1* (m1) and *CHRM2* (m2), respectively, and a very small proportion of ~0.5-0.7% (< 100 nuclei) of all cells expressed *CHRM4* (m4). Within each *CHRM*-expressing subpopulation, >90% of the *CHRM*+ cells were neurons, with ~61-82% ExNs and 18-33% InNs (Supplementary Fig. 1L), but the degree of neuronal versus non-neuronal expression was dependent on the specific *CHRM* gene, with *CHRM3* having highest proportion expressed in the non-neuronal cells.

Examination of mAChR gene enrichment within each major cell type revealed that *CHRM3*+ neurons comprise 89-91% of total ExN and ~76% of total InN in both areas (Fig. 1F). In contrast, only 10-14% and 16-20% of all neurons expressed *CHRM1* and *CHRM2*, respectively (Fig. 1F). *CHRM1* and *CHRM2* were barely detectable in a small proportion of non-neuronal cells (0–2% for *CHRM1* and 0 -4% for *CHRM2*). *CHRM4* was exclusively expressed in neurons. In contrast, *CHRM3* was expressed in 14-17% of total oligodendrocytes, 6-8% of total OPCs, 6-8% of total astrocytes and 5-7% of total microglia (Fig. 1F). Further, when comparing expression levels of *CHRM1-4* within each cell type, we found that the two areas were also largely similar, except for *CHRM3*+ ExNs. Within the population of ExNs, *CHRM3* was significantly upregulated in LPFC, with slightly higher average *CHRM3* expression level, relative to ACC (Fig. 1C, adjusted $p < 0.05$).

Acetylcholine also exerts its effects through the ionotropic ligand-gated nicotinic receptors (nAChRs) [reviewed in[9,10]]. Our analyses found that mAChR genes *CHRM1-3* were expressed at

ARTICLE IN PRESS

ARTICLE IN PRESS

higher levels (greater cell enrichment and expression level per cell) than nAChR subunit genes in both ACC and LPFC (Supplementary Fig. 1M). For nAChR genes, the most predominantly expressed subunit in both areas was *CHRNA7*, which encodes for the nAChR alpha7 subunit. *CHRNA7* was mainly expressed in neurons in both areas (~21% of ExNs and 27-30% of InNs), and in a small proportion of non-neuronal cells depending on area and class (~3% of astrocytes and ~9% of OPCs of both areas; ~6% and 12% of microglia, in ACC and LPFC respectively; ~11% of pericytes/other cells in ACC; Supplementary Fig. 1M). Other nAChR genes were expressed at very low levels in a small proportion of cells (<1% of cells), except for *CHRNB2* which was expressed in 7-9% of ExNs and 3-4% of InNs, and *CHRNA2* which was expressed in ~4% of InNs (Supplementary Fig. 1M). This pattern is somewhat unexpected, since α4 and ß2, along with α7, are among the highest expressed nACHR subunits based on receptor radioligand binding assays and *in situ* hybridization labeling in macaque cortical tissue [48-50]. Nonetheless, our current data confirmed that, at the transcript level, mAChRs are the predominant cholinergic receptor class expressed in these frontal areas. Importantly, these expression patterns are consistent with previously published single-cell transcriptomic datasets in macaque and human cortex[51-53] (Supplementary Fig. 1N).

Predominant nuclear mRNA localization and mRNA:protein correlation in m3+ expressing neurons

The widespread expression of *CHRM3* compared to other mAChR subtype genes did not align with previous studies at the protein level, which showed that m1 is the most predominantly expressed mAChR subtype in the cortex[47]. Thus, histological validation of m1 and m3 mRNA-protein expression was employed using combined IHC and fluorescence *in situ* hybridization (FISH, Fig. 1G-L; n = 4 monkeys, Supplementary Table 3). Stereological quantification in layers

ARTICLE IN PRESS

2-3 (L2-3) confirmed a significantly greater density of m1+ protein expressing cells compared to m3+, specifically in ACC (m1 v m3, Welch's t-test, ACC L2/3: $t(5) = 4.477$, $p = 0.0056$ and LPFC L2/3: $t(4.834) = 2.281$, $p = 0.0732$; Fig. 1H). Further, we found that m1+ protein mean intensity per cell was significantly higher than m3+ in both areas (m1 vs. m3, Welch's t-test, ACC: $n = 3013$ cells, $t(5790) = 24.97$, $p < 0.0001$ and LPFC: $n = 3344$ cells, $t(5631) = 10.12$, $p < 0.0001$ from 4 monkeys; Fig.1I), consistent with previous qualitative data in other cortices[54]. In contrast, mRNA mean intensity differed significantly only in LPFC, with m3 mRNA having greater mean intensity than m1 (m1 vs. m3, Welch's t-test, LPFC: $t(6686) = 5.075$, $p < 0.0001$, ACC: $t(5725) = 1.599$, $p = 0.1099$; Fig. 1I). Among all m1+ protein expressing neurons, 61-73% in ACC and 62-64% in LPFC also expressed *CHRM1*+ mRNA (Fig, 1J, mRNA+/prot+, dark gray). Conversely, 27-39% in ACC and 36-38% in LPFC of these m1+ neurons expressed the m1 protein but not *CHRM1* (Fig. 1J, mRNA-/prot+, open bars). Almost all m3+ protein expressing neurons (~ 88-95% in ACC and 95-96% in LPFC) also expressed *CHRM3* (Fig, 1I, mRNA+/prot+, dark gray). In marked contrast to m1+ neurons, we found a significant proportion of neurons with detectable *CHRM3* mRNA that were negative for m3 protein (ACC: L2-3 = 29%, L5-6 = 15%; LPFC: L2-3 = 17%, L5-6 = 19%; Fig. 1J, mRNA+/prot-, cyan).

Given these differences between m1 versus m3 protein and mRNA co-expression, we assessed the correlation between protein and mRNA levels within individual m1 and m3 expressing neurons (Fig. 1K). For m3+ cells in both ACC and LPFC, we found a significant positive correlation between mRNA and protein particle density (ACC: Pearson's $r = 0.2408$; LPFC: $r = 0.1871$; $p < 0.0001$). For m1+ cells, mRNA and protein expression was only correlated in LPFC ($r = 0.23567$; $p < 0.0001$) but not in ACC ($p = 0.3792$). These relationships suggest region-

ARTICLE IN PRESS

specific differential mRNA and protein dynamics in m1 vs m3 neurons, with mRNA and protein being more strongly correlated in m3 compared to m1 expressing neurons, especially in the ACC.

While the mRNA mean intensity per cell was similar for m1 and m3 expressing cells, our analyses revealed a marked difference in intracellular localization of *CHRM1* vs. *CHRM3* mRNA (Fig. 1G, L). Most *CHRM1* was localized to the cytoplasm, with weak or no labeling in the nucleus (% cytoplasmic, ACC: 61-64%; LPFC: 66-71% of m1 mRNA+ cells; Fig. 1G, L). In contrast, *CHRM3* was detected in both the nucleus and cytoplasm of all cells (% nuclear + cytoplasmic, ACC: 95-97%; LPFC: 98-100% of m3mRNA+ cells). These data suggest differences in the mechanisms regulating mRNA export and translation between the mAChR subtypes.

CHRM1-4 mRNA was widely co-expressed in patterns that differed across layer-specific ExN subpopulations

Differential gene expression (DEG) and marker enrichment analyses between ACC vs. LPFC revealed region-specific transcriptional signatures within total ExNs (Fig. 2A, B). Functional annotation analyses via EnrichR[55-57] revealed that genes enriched in ACC area 24 ExNs were mainly associated with glutamatergic signaling and synapse formation. These include genes for glutamate receptors subunits (*GRID1, NR2B*), glutamatergic synapse adhesion (*NRXN1, NLGN1*[58]) and scaffolding (*PPFIA2, DMD, TANC, LRRC7*[59-62]; Fig. 2A, B; Supplementary Data 1). LPFC area 46 ExNs exhibited relative enrichment of genes related to G-protein coupled receptor signaling pathways specifically involved in cholinergic signaling (*CHRM3* and *PLCB1*[63]), K channel activity (*KCNIP4*[64]) and protein homeostasis (*FBXL17*[65,66]; Fig. 2A, B; Supplementary Data 1). These data suggest regional transcriptional specialization in GPCR-related signaling machinery. Interestingly, both areas showed enrichment of genes and functional terms associated with development and plasticity, but this enrichment is more robust in ACC (with more

ARTICLE IN PRESS

significantly enriched genes and terms) compared to LPFC (Fig. 2A, B; Supplementary Data 1). Further, the few plasticity-related genes enriched in LPFC mainly promote dendrite and synapse stability (e.g. alpha N-catenin genes, *CTNND2, CTNNA2* which inhibit filopodia formation[67-69]). In contrast, ACC plasticity-related genes are involved in both spine motility (*GPM6A* which promotes filopodia formation[70,71]) and promoting glutamatergic synapse stability (e.g. *NRXN1, NLGN1*[58]).

Among ExNs, LPFC exhibited a greater fold-change expression of *CHRM3* compared to ACC (see Fig. 1C). However, when we assessed the relative proportion of ExNs expressing/co-expressing *CHRM1-4*, we found a similar distribution in ACC and LPFC. Within both areas, the majority (~60%) of ExNs expressed *CHRM3* only (Fig. 2C, dark blue). The second largest population, consisting of 27-28% of all ExN, were those co-expressing two or more mAChRs (Fig. 2C, dark grey). The rest of the ExN population was comprised of ~4% *CHRM2+* only, and 5-7% with no mAChR gene expression (Fig. 2C, orange and light grey, respectively). We found no ExNs that exclusively expressed *CHRM4*, as it was always co-expressed with another mAChR gene.

More granular transcriptomic analysis of ExN subpopulations via re-clustering of cell types annotated as ExN, revealed differences in *CHRM1-4* expression/co-expression patterns associated with expression of layer-specific genes. The re-clustering analysis yielded 11 clusters of ExNs (Fig. 2C, D, G; Supplementary Fig. 2A-E) distributed and annotated based on distinct expression of layer-specific genes[72-75] (Fig. 2D, Supplementary Fig. 2A-E, Supplementary Table 2). For the largest subpopulation of upper layer (UL) 2-3 ExNs, ~80% of neurons expressed only *CHRM3*, and ~20% co-expressed two or more mAChR*s* (Fig. 2I, dark blue). Layer 4 ExN cluster expressed either only *CHRM3* or co-expressed mAChRs, with a more equal distribution (60-40% ratio; Fig. 2I). Similarly, 45-60% of UL3b ExNs expressed only *CHRM3* and the rest either co-expressed >2

ARTICLE IN PRESS

mAChR*s* (20-30%) or did not express any mAChR (20-25% of ExN; Fig. 2I). While the deep layer (DL) L5-6 ExN cluster also included ~50-60% ExNs expressing only *CHRM3,* this subcluster was uniquely enriched with ExNs expressing only *CHRM2* (20-30% of DL5-6 ExN, sub-cluster 7; Fig. 2I, orange). In contrast to other clusters, the UL1-2 ExN cluster had a relative enrichment of cells (~40-60%) that did not express any mAChR (of total UL1-2 ExNs; Fig. 2I).

Further analyses of the specific combinations of *CHRM1-4* co-expression revealed layer-specific ExN distribution patterns among subpopulations (Fig. 2J). The majority of ExNs in UL1-2, UL2-3 and DL5-6 clusters in both areas, co-expressed *CHRM1+*/*CHRM*3+ (Fig. 2J, light blue). In contrast, ExN L4 clusters with mAChR co-expression were predominantly *CHRM2+/CHRM*3+ (Fig. 2J, light orange). Interestingly, DL5-6 ExNs in both areas had a relatively higher proportion of cells co-expressing *CHRM1+*/*CHRM*2+ as compared to other clusters (2-3% in DL5-6 vs < 0.5%; Fig. 2J, dark orange). Within all ExN subpopulations, < 5% co-expressed *CHRM4* with *CHRM1-3*. These results show distinct patterns of mAChRs mRNA enrichment and co-expression across layer-specific ExN subtypes.

Patterns of mAChR subtype mRNA expression/co-expression distinguished two broad groups of InN subpopulations

Similar to ExN, most (~56%) of the InN in ACC and LPFC expressed only *CHRM3* (Fig. 2E, dark blue), while the rest (~19-21%) co-expressed two or more mAChRs (Fig. 2E, dark grey) or had no mAChR expression (Fig. 2E, light grey). A very small proportion of InN were either only *CHRM2+* (2% in LPFC vs 4% of ACC) or *CHRM1+* (2.4% in LPFC vs 2.8% of ACC; Fig. 2E). Interestingly, in contrast to ExNs, we found < 0.5% of InNs exclusively expressing *CHRM4*.

Analyses of InN subpopulations via re-clustering revealed 8 subclusters that were distributed and annotated based on the expression of neurochemically distinct InN genes [76-80] (Fig.

ARTICLE IN PRESS

ARTICLE IN PRESS

2F, H; Supplementary Fig. 2F-J). Specifically, parvalbumin (*PVALB+,* consist of cells from clusters 1 and 5), somatostatin (*SST+,* cluster 0), vasoactive intestinal peptide (*VIP+,* cluster 2) , cholecystokinin (*CCK,* cluster 3) expressing neurons formed distinct clusters (Fig. 2F). A subset of *SST*+ neurons (cluster 6) co-expressed calbindin (C*ALB1*), *VIP,* and *CCK* (Fig. 2F). Clusters 4 and 7 did not exhibit predominant expression of any of the neurochemical markers examined here and were excluded from subsequent analyses.

Our data revealed that the patterns of mAChR expression/co-expression differentiated neurochemically distinct InNs cell types. Specifically, for all neurochemical subclusters, except *PVALB+,* >50% of InN consisted of only *CHRM3+*. *PVALB+* InN cluster had the lowest proportion of only *CHRM3+* (30-35% of *PVALB+* InN; Fig. 2I, dark blue) and the highest expression of only *CHRM2+* (15%, Fig. 2I, orange). Further, our dataset revealed two distinct mAChR co-expression patterns, distinguishing two major groups of InNs (Fig. 2J). The first group consisted of *PVALB+, CCK+, CALB1+,* and *SST+* InNs, which mainly co-expressed *CHRM2+/CHRM3+* (54-64% in ACC; 53-67% in LPFC; Fig. 2J, orange). In contrast, the second group, consisted of *VIP+* and *CALB2+* InNs, predominantly co-expressing *CHRM1+/CHRM3+*, and these InNs were more enriched in ACC than in LPFC (67% in ACC vs 42% in LPFC of *VIP+*; and 75% in ACC vs 45% in LPFC of *CALB2+* InNs; Fig. 2J, light blue).

Differentially expressed genes (DEGs) across CHRM1-3 enriched neurons show functional overlap of m1 and m3, and their distinction from m2

To assess whether mAChR gene expression was correlated with distinct transcriptomic profiles related to receptor-specific downstream effectors, we identified DEGs cross *CHRM1-3* enriched ExN and InN subpopulations within each region. For this purpose, we performed pseudobulk analysis of the total ExN and total InN cell types and identified DEGs for the following

ARTICLE IN PRESS

comparisons: *CHRM1*+ vs. *CHRM2+; CHRM3*+ vs. *CHRM2*+, and *CHRM1*+ vs. *CHRM3*+ *(*Fig. 3A; Supplementary Fig. 3). Overall, these data indicated that *CHRM1*+ and *CHRM3*+ neurons had largely similar transcriptomic profiles that were distinct from that seen in *CHRM2*+ neurons. *CHRM1*+ *vs. CHRM2*+, and *CHRM3*+ *vs. CHRM2*+ comparisons resulted in a high number of DEGs genes in both ACC and LPFC ExNs and InNs (Fig. 3A). In contrast, *CHRM1*+ vs. *CHRM3*+ yielded almost no DEGs in ExNs (1 DEG for each area) and a very a low number of DEGs in InNs (ACC 6, LPFC 25; Fig. 3A, Supplementary Data 2). Interestingly, the degree of similarity between *CHRM1*+ and *CHRM3*+ seemed to be more pronounced for ExNs compared to InNs. For InNs, *CHRM3*+ vs. *CHRM2*+ resulted in a higher number of DEGs as compared to *CHRM1*+ vs. *CHRM2*+ for both areas (ACC 60 vs. 19; LPFC 59 vs. 24 DEGs, respectively; Fig. 3A), suggesting receptor-specific differences between *CHRM1*+ and *CHRM3*+. Further, the ExN populations revealed region-specific distinctions in the number of DEGs. In the ACC ExNs, *CHRM1*+ vs. *CHRM2*+, and *CHRM3*+ vs. *CHRM2*+ yielded a comparable number of DEGs (65 vs. 76 DEGs, respectively; Fig. 3A). However, in LPFC ExNs, the number of DEGs was slightly higher for *CHRM3*+ vs. *CHRM2*+ compared to *CHRM1*+ vs. *CHRM2*+ (51 vs. 35 DEGs, respectively; Fig. 3A).

To evaluate how distinct transcriptomic profiles of mAChR expressing cells relate to function, we utilized functional annotation analyses using KEGG pathway[81,82], and gene ontology (GO) analysis[83,84] in EnrichR[55-57]. For ExNs, EnrichR analysis of DEGs from *CHRM1*+ vs. *CHRM2*+ and *CHRM3*+ vs. *CHRM2*+ comparisons yielded similar significantly enriched ($p < 0.05$) KEGG pathway and GO terms for biological processes in both areas (Fig. 3B-F, Supplementary Data 3 and 4). The top enriched terms had overlapping gene sets related to four major functions: synaptic transmission (e.g. Glutamatergic Synapses, Chemical Synaptic

ARTICLE IN PRESS

Transmission, Synapse Organization; Fig. 3B-D), calcium signaling (Ca^{2+} Signaling, Ca^{2+} Ion Transport, Fig. 3B,C,E), axon guidance/plasticity and development (Axonogenesis, Neuron Projection Guidance, Cell Adhesion, MAPK2 and RAP1 pathways that regulate cell polarity and growth Fig. 3B,C,F)[85,86]. Significantly enriched terms were also related to cAMP/cGMP, G-protein coupled signaling (Fig. 3B-F), consistent with the opposite physiologic effects of the m1/m3 vs m2 receptors on second messenger cascades[87-89].

These enriched functional terms common to ACC and LPFC were derived from overlapping *CHRM1+/3+* vs. *CHRM2+* ExN DEGs, which included genes for glutamatergic receptors, Ca^{2+} and K+ channels, and genes related to second messenger cascades (Fig. 3D, E). The top *CHRM3+* genes (relative to *CHRM2+)* in ExNs included *GRIA2 and GRIA3 (*ionotropic glutamate receptor genes), *CACNA1E (*R-type Ca^{2+} channel) *ADCY1* adenylyl cyclase 1, while some of the top *CHRM2+* enriched genes included *HTR2C* (serotonergic receptor), *GIRK1* (inwardly-rectifying K+ channel), and *GRM3* and *GRM4* (metabotropic glutamate receptors). In both areas, *CHRM2* enrichment in ExNs was associated with positive regulators of synapse maturation and stability genes *(UNC5D, EPHA5/7*[90]*, SEMA3A* [91]*, DCC* [92]*, TRPC3* [93]*).*

In addition to gene sets that were consistent between areas, there was a small subset of *CHRM3+* vs. *CHRM2+* DEGs encoding for adenylyl cyclases, glutamatergic receptors and calcium channels, which were unique within ACC and LPFC ExNs (Fig. 3D, E). For instance, two distinct differentially expressed adenylyl cyclases were associated with each region: In ACC, *ADCY1* the subtype responsive to calcium calmodulin[94], was enriched in *CHRM3+* ExNs, while in LPFC *ADCY2*[95] was enriched in *CHRM2+* ExNs (Fig. 3E). For Ca^{2+} channels, ACC *CACNA1A*, which encodes for a P/Q-type Ca^{2+} channel concentrated in presynaptic terminals, and LPFC *CACNA1C*, which encodes for an L-type Ca^{2+} channel in somatodendritic domains[94], were

ARTICLE IN PRESS

enriched in *CHRM2*+ ExNs (Fig. 3D, E). In addition, *CHRM3*+ vs. *CHRM2*+ DEGs related to axon guidance, adhesion and plasticity, showed a relatively high proportion in ACC compared to LPFC (Fig. 3F). Specifically, ACC ExNs had a higher representation of *CHRM3*+ vs. *CHRM2*+ DEGs linked to the ROBO pathways, mediating axon guidance and adhesion, as compared to LPFC (Fig. 3F, *ROBO1* and *SLIT1/2/3*, *SEMA5A*)[96-98].

Similar to ExNs, functional annotation analyses of DEGs associated with *CHRM1-3* expression in InNs within each area yielded significantly enriched terms related to Ca^{2+} signaling, chemical synaptic transmission and plasticity (Fig. 3G-J). While the number of DEGs across *CHRM1-3* expressing InNs was smaller in comparison to ExNs, the fold change for each gene was greater. Similar to ExNs, the number of *CHRM3*+ vs. *CHRM2*+ InN DEGs related to plasticity was greater in ACC than in LPFC, which included genes associated with presynaptic specialization assembly (*ROBO2, TNEM1*)[96-99] and RNA dynamics important for synapse development (*RBFOX1/3, SOX6*)[100,101].

The analyses showed unique DEGs yielded by *CHRM1*+ vs. *CHRM2*+ and *CHRM3*+ vs. *CHRM2*+ comparisons, especially in LPFC InNs. For instance, the term 'chemical synaptic transmission' included DEGs related to GABAergic and glutamatergic receptors in LPFC *CHRM1*+ vs. *CHRM3*+ InNs, but related to Ca^{2+} Channels, K channels and synapse structure in LPFC *CHRM3*+ vs. *CHRM2*+ InNs (Fig. 3J, Supplementary Data 2 and 3). These data further support the transcriptomic heterogeneity of *CHRM1*+ vs. *CHRM3*+ InNs, driven primarily by neurotransmitter specificity, that was not found for ExNs.

Taken together these data indicate that distinct *CHRM* enrichment within both ACC and LPFC correlates with transcriptomic signatures linked to key signaling cascades, in patterns

ARTICLE IN PRESS

consistent with the functional overlap between m1 and m3 mAChRs that are distinct from m2. Further, the degree of this m1 and m3 functional overlap is more pronounced in ExNs than in InNs.

Greater number of DEGs between ACC and LPFC for CHRM1-3 enriched ExN than for InNs

Within each *CHRM*+ neuron subpopulation, between-region differential gene expression analyses revealed that ExNs exhibited greater regional differences compared to InNs. We identified higher numbers of between-region DEGs for *CHRM1*+, *CHRM2*+, and *CHRM*3+ ExNs (140, 93, and 204 DEGs, respectively) compared to *CHRM2*+, and *CHRM3*+ InNs (no DEGs for *CHRM1*+, 8 for *CHRM*2+, and 37 for *CHRM3*+; Fig. 4A-C, see Supplementary Data 4).

ARTICLE IN PRESS

EnrichR analysis based on between-region DEGs revealed significant enrichment in KEGG pathways and GO terms that were markedly similar between *CHRM1*+ and *CHRM3*+ ExNs (Fig 4D-F). The top common terms enriched in ACC were related to synaptic plasticity (axon guidance, cell-to-cell adhesion and chemical synaptic transmission; Fig 4D-F). ACC-upregulated DEGs associated with axon guidance and cell-to-cell adhesion, included genes coding for the ROBO pathway components (*ROBO1/2, SLIT3, SEMA3A*), cadherins (*CDH6/4/9/10/13*), teneurins (*TNEM1/2/3*), ephrin signaling components (*EPHA6/7/3,*) and some other scaffolding and adhesion proteins (*NLGN1, DCC, UNC5D)*; Fig. 4G, H) for synapse formation[90,91,96-99,102]. Related between-area DEGs were associated with chemical synaptic transmission (Fig. 4D, d inset, 4F, f inset, and 4I), which included glutamate receptors (*GRIA1/4, GRIN2B/3A, GRID2, GLRA2*), GABA receptors (*GABRA3/5/2*), synaptic structural and adhesion proteins (*NLGN1, ERC1*) and Ca^{2+} channels (*CACNA1E/B2*). In addition, *CHRM1*+ ExN between-region DEGs showed the unique enrichment for RAP1 signaling and Long-Term Potentiation (LTP) terms that are important for synapse plasticity[103-106] (Fig. 4D). Between-region DEGs in *CHRM1+/3*+ ExNs, which were associated with synaptic function and plasticity, were primarily upregulated in ACC compared to

ARTICLE IN PRESS

LPFC (Fig. 4D, d inset, 4F, F inset, and 4I). Interestingly, we found that most of the ionotropic glutamate receptor genes were ACC-enriched (relative to LPFC), while GABAergic receptor genes had mixed trends. For *CHRM3*+ ExNs, *GABRA3/5/2* and *GABBR1* genes were ACC-enriched, but *GABRB2, GABBR2 and GABRAG3* were enriched in LPFC (Fig. 4F, f inset).

Similar to *CHRM*3+/*CHRM1*+ ExNs, a subset of significantly enriched KEGG pathway and GO terms found for *CHRM2*+ ExN ACC vs LPFC DEGs were related to Ca^{2+} signaling, glutamatergic signaling, oxytocin signaling, nicotine, cAMP, adhesion, and development (Fig. 4E). However, we found terms unique to *CHRM2*+ ExNs related to Na+ ion transport and Long-Term Depression (LTD) (Fig. 4E). These DEGs were mostly ACC-enriched relative to LPFC, which included *PDEA1*, the gene for phosphodiesterase 1 (a modulator of cAMP/cGMP activity), and *SCN9A* (Na channel gene) and *PRKG1* (cGMP-dependent protein kinase gene), which are implicated in nociception[107,108] (Fig. 4E, e1, e2, insets). Importantly, *GRID2* and *GRIA1* genes for ionotropic GLUR delta type subunit 2 and GLUR AMPA type subunit 2, respectively, were consistently enriched in ACC relative to LPFC across *CHRM*+ expressing ExNs (Fig. 4D-I).

In contrast to ExNs, the comparison between ACC vs. LPFC among the *CHRM*+ InN population yielded a markedly lower number of DEGs, with significantly enriched GO terms only for *CHRM*3+. Similar to ExNs, we found a significant enrichment in the processes related to cell-cell adhesion and trans-synaptic signaling for between-region DEGs in *CHRM*3+ InNs (Fig. 4J). The genes upregulated in ACC *CHRM*3+ InNs (relative to LPFC) included cadherins (*CDH4*), genes encoding for synaptic adhesion (*NLGN4Y, NRXN1, CADM1*), and presynaptic (*UNC13B*) and postsynaptic (*GRIA1, GIRK2, GLRA3*) specializations (Fig. 4J, j inset; Supplementary Data 4). These findings reveal region and cell-type specific transcriptomic differences as they pertain to *CHRM1-3* enrichment.

ARTICLE IN PRESS

Functional experiments demonstrated differential effects of CCH on synaptic properties in ACC and LPFC

Our transcriptomic profiling revealed changes in genes related to synapse stability that were upregulated in ACC relative to LPFC. Thus, we investigated differences in synaptic properties between the two areas (Fig. 5; Supplementary Fig. 4). We assessed the effects of the cholinergic agonist, carbachol (CCH), on synaptic currents and structural measures of synaptic plasticity in layer 3 (L3) pyramidal neurons in ACC and LPFC using whole-cell patch clamp recording and intracellular filling. Recordings of spontaneous excitatory and inhibitory post-synaptic currents (EPSC and IPSC) were obtained from L3 pyramidal neurons of ACC (n=20 EPSC from 9 cases, n=16 IPSC, from 7 cases) and LPFC (n=14 EPSC, n=10 IPSC, from 7 cases), following 6-8 min bath exposure to CCH (10µM; Fig. 5A-E; and Supplementary Fig. 4A, B). In both frontal areas, most cells exhibited a decrease in the frequency of EPSCs (60% in ACC, 50% in LPFC), defined as cells exhibiting 20% or more lower frequency from baseline after CCH ($p < 0.05$ repeated measures ANOVA for time histogram of number of events; and $p < 0.05$, K-S test of inter-event-interval distributions; Fig. 5D, F, G). The remaining cells from each area exhibited either an increase (> 20% increase from baseline) or no change in frequency, which consist of 25% and 15% respectively of cells in ACC (Fig. 5F, G). In LPFC, ~37% of cells exhibited an increase, while 13% showed no change in frequency after CCH (Fig. 5F, G). We performed a Two-way ANOVA to assess the main and interactive effects of area x drug on properties of synaptic currents. Our analyses revealed a main effect of drug on EPSC frequency ($F(1, 66) = 6.41$, $p = 0.0137$), with no significant interactive effects and no other differences found in amplitude or kinetics (Fig. 5H, Supplementary Data 5). Specifically, CCH significantly decreased the mean EPSC frequency, specifically in ACC neurons (CTR v CCH, Fisher's LSD post-hoc, p=0.012; Fig. 5H). This data

ARTICLE IN PRESS

suggests a predominantly presynaptic effect of CCH, suppressing neurotransmitter release from excitatory axon terminals in ACC.

Analysis of IPSCs revealed heterogeneity in the CCH effect between the two areas (Fig. 5E, I, J). In the ACC, majority (53%) of recorded cells exhibited a CCH-related increase in IPSCs frequency, while 29% had a decrease, and 18% exhibited no change from baseline (Fig. 5I). By contrast, in the LPFC, majority (50%) of recorded cells exhibited a CCH-related decrease in IPSC frequency, while 33% displayed an increase, and 17% exhibited no change from baseline (Fig. 5I). Two-way ANOVA (area x treatment) revealed a significant main effect of area on IPSC frequency ($F(1, 60)= 11.19$, $p = 0.001$) and total charge transfer ($F(1, 60)= 7.34$, $p = 0.009$), which were significantly higher in ACC compared to LPFC, specifically in the CCH group (ACC vs LPFC: Fisher's LSD post-hoc, frequency $p=0.001$; total charge $p =0.006$; Fig. 5J, Supplementary Data 5). In addition, we found a significant main effect of drug treatment ($F(1, 60)= 4.65$, $p = 0.034$) and a trending interactive area x treatment effect ($F(1, 60)= 3.62$, $p = 0.06$) on IPSC frequency. Specifically, within ACC, CCH significantly increased IPSC frequency compared to baseline control (CCH v CTR, Fisher's LSD post-hoc, $p = 0.004$; Fig. 5J). Interestingly, we also found a significant main effect of drug treatment on IPSC amplitude ($F(1, 56)= 5.62$, $p = 0.02$), with CCH significantly decreasing IPSC amplitude only in LPFC (CTR vs CCH, Fisher's LSD post-hoc, $p=0.01$, Fig. 5J).

Due to the CCH suppression of EPSCs and increased IPSCs in ACC, we found that the total excitatory to inhibitory charge transfer (E:I) ratio was significantly lower in ACC than in LPFC neurons, specifically after CCH exposure (main effect area, $F(1, 45) = 4.64$, $p=0.03$; area x drug interaction, $F(1, 45) = 5.2$, $p = 0.027$; ACC v LPFC CCH, Fisher's LSD post-hoc, $p = 0.005$; Fig. 5K, Supplementary Data 6). Scatter plots of EPSC versus IPSC for ACC and LPFC showed that,

ARTICLE IN PRESS

ARTICLE IN PRESS

in ACC neurons, after CCH exposure, the E:I ratios were <1, suggesting a shift towards a predominance of inhibition over excitation (Fig. 5L). In LPFC, there was an overlap between control and CCH conditions, with majority of the cells dominated by excitation after CCH treatment (Fig. 5L).

Control washout experiments in a subset of cells (n=2/6 ACC cells from 4 cases; and n=1/3 LPFC cells from 2 cases), demonstrated the reversal of CCH effects on EPSC and IPSC frequency after 15 min of washout (Supplementary Data 5, Supplementary Fig. 4A, B). However, we also found heterogeneity in the washout responses, with only about a third showing this reversal/partial reversal of the CCH effects after 15 min washout in Ringer's (Supplementary Data 5, Supplementary Fig. 4C-F). About a third of the cells were CCH-responsive yet did not exhibit a washout effect, and the remaining third did not exhibit changes in EPSC/IPSC frequency after 8 min of CCH and instead showed a significant difference between baseline and washout (Supplementary Data 5, Supplementary Fig. 4C-F, $p < 0.05$, repeated measures ANOVA of events over time). These data suggest that the time course of CCH effects can differ across cells, with some exhibiting transient, sustained or delayed responses to CCH.

Previous studies in rodents and cultures show that cholinergic activation can modulate plasticity of spines – the postsynaptic sites of excitatory synapses[109-111]. We therefore assessed spine density and morphology, which reflect different states of plasticity[102,104-106,112], on apical and basal dendrites of L3 pyramidal neurons in slices treated with control Ringer's solution (n = 15 ACC cells, 9 LPFC cells from 7 cases), 8 min of 10 μM CCH (n = 5 ACC cells from 2 cases, 4 LPFC cells from 3 cases), or 10 min of CCH followed by 15 min of washout in Ringer's solution (n = 3 ACC cells, 6 LPFC cells from 2 cases; Fig. 6). A two-way ANOVA (area x treatment) revealed a significant main effect of treatment (CTR v CCH v washout; $p < 0.05$) on subtype

ARTICLE IN PRESS

distribution and size of spines on apical and basal dendrites of ACC and LPFC neurons (Fig. 6A). In both areas, compared to control, CCH-treated neurons had significantly lower mean densities of mushroom and stubby spines mainly on apical dendrites (main effect treatment, density mushroom $F(2, 36) = 6$, $p = 0.006$; stubby $F(2, 36) = 9.76$, $p = 0.0004$; CTR v CCH Fisher's LSD post-hoc $p < 0.05$; Fig. 6A-B, Supplementary Data 6). Accordingly, there was a decrease in the proportion of mushroom and stubby spines and a concomitant increase in the proportion of thin spines in CCH-treated compared to control neurons both areas, but the effect was more prominent in LPFC (main effect treatment, proportions: mushroom $F(2, 36) = 5.87$, $p = 0.006$; stubby $F(2, 36) = 7.32$, $p = 0.002$; thins $F(2, 36) = 14.69$ $p = 0.00002$; Fig. 6C). Similar differences between CCH vs control neurons were found in basal dendrites, albeit to a lesser extent, with significant between-treatment differences in the percent of thin and stubby spines observed in LPFC, and in the density of mushroom spines in ACC (main effect treatment, % stubby $F(2, 34) = 4$, $p = 0.03$; % thins $F(2, 34) = 3.6$, $p = 0.04$; mushroom density $F(2, 34) = 4.22$, $p = 0.02$; Fig. 6A-C, Supplementary Data 6).

Significant between-area differences in spine densities were found mainly in basal dendrites. Specifically, the densities of total and thin basal spines were greater in ACC compared to LPFC neurons in the control and CCH groups (main effect area, total spines $F(2, 34) = 13.15$, $p = 0.0009$, thin spines $F(2, 34) = 12.41$, $p = 0.001$; Fisher's LSD post-hoc $p < 0.05$; Fig. 6A, Supplementary Data 6). However, for mushroom spine densities, a main effect of area was significantly found for both apical and dendrites, with ACC neurons having greater mushroom spine densities compared to LPFC, specifically in control and washout groups (main effect area, apical $F(2, 36) = 8.13$, $p = 0.007$; basal $F(2, 34) = 9.73$, $p = 0.004$; Fisher's LSD post-hoc $p < 0.05$, Supplementary Data 6; Fig, 6A)

ARTICLE IN PRESS

ARTICLE IN PRESS

Between-drug treatment differences were also found for spine size, with smaller head diameter of mushroom spines in CCH compared to control neurons in apical dendrites of ACC and basal dendrites of LPFC (apical main effect $F(2, 36) = 2.23$, $p = 0.03$; interaction treatment x area, $F(2, 36) = 3.83$, $p = 0.03$; basal main effect $F(2, 34) = 4.99$, $p = 0.01$; interaction treatment x area $F(2, 34) = 3.41$, $p = 0.04$; CCH vs CTR Fisher's LSD post-hoc: $p < 0.01$, Fig. 6D). Interestingly, these CCH-associated patterns of spine distribution and size seemed to persist even after 15 min washout (Fig. 5A, C, D). However, with regards to spine head diameter, there was an opposite pattern of washout effect in ACC vs LPFC (Fig. 5D). While both areas exhibited a decrease in spine head size of mushroom spines after CCH, ACC cells exhibited a reversal of this CCH-related decrease in spine head diameter after 15 min washout (CTR vs washout, Fisher's LSD post-hoc, $p = 0.32$; Fig. 5D, Supplementary Data 6). In contrast, LPFC cells showed a persistence of this CCH effect, with washout condition significantly different form control baseline ($p = 0.017$) but not CCH ($p = 0.45$; Fig. 5D, Supplementary Data 6). Overall, these data suggest that cholinergic stimulation with CCH can lead to shifts in spine morphology and plasticity[102,104-106,112], and that short versus long term effects of CCH on these parameters and related synaptic functional properties may differ across areas and cell types.

Discussion

The current study expands on our previous findings[40] through comprehensive transcriptional profiling of *CHRM1-4* expressing neurons and parallel assessments of protein vs. mRNA expression and related physiological effects of cholinergic stimulation of ACC vs. LPFC. Our snRNA-seq analysis of mAChR gene expression across neuronal subtypes in the macaque frontal cortex revealed intriguing patterns that both align with and diverge from previous protein-

ARTICLE IN PRESS

level studies[47,113,114]. Consistent with earlier work[40,41], we found that most cortical neurons co-express mAChR subtypes at the protein and mRNA level. However, the gene expression hierarchy (*CHRM3* > *CHRM2* > *CHRM1*) contrasts with the protein-level predominance of m1 receptors in the cortex, as shown by our m1+/m3 protein quantification here and in previous work[40,54]. Indeed, we found that m1+ protein expression level within individual cells is greater than m3+. However, it is important to note that the abundance of m1+ vs m3+ protein-expressing cells are more comparable to each other than previously thought based on qualitative/semi-quantitative estimates[54]. In fact, majority of neurons in L2-3 of both areas co-express m1 and m3 proteins, and the total density of m1+ neurons was only marginally (~20%) greater than m3+ neurons. Our estimates are in line with more recent autoradiographic studies showing that m3 and m1 receptor binding density in macaque parietal cortex are equivalent[115].

As summarized in Figure 6E, the present study reveals a novel mRNA-protein discrepancy for m3 expression in ACC and LPFC, which highlights the complex relationship between transcription and translation. Recent research has shown that actively transcribed genes may have fewer RNA copies due to instability, while more stable transcripts can accumulate long after transcription has ceased (reviewed in [116,117]). Our combined IHC and FISH experiments revealed a higher proportion of cells expressing m1 protein without detectable *CHRM1*, which could indicate dynamic mRNA transport and turnover with a more stable and longer protein half-life[118]. These data are consistent with recent work in macaques showing a lack of correlation between *CHRM1* mRNA and autoradiographic measures of M1 receptor density[119]. Further, the m1 receptor has been shown recently to undergo SUMOylation, which increases protein stability and cell surface expression[120]. Conversely, our finding of *CHRM3* presence in cells lacking detectable m3 protein suggests dynamic regulation and rapid turnover of protein expression[121]. Specific

ARTICLE IN PRESS

ARTICLE IN PRESS

phosphorylation patterns can promote receptor internalization, leading to either recycling or degradation, thus impacting overall receptor abundance[122]. Notably, our data revealed that the subcellular localization patterns of *CHRM1* and *CHRM3* transcripts differed. The predominant cytoplasmic localization of *CHRM1* suggests active translation, while the primarily nuclear localization of *CHRM3* implies regulatory mechanisms involving mRNA retention due to the interaction with RNA-binding proteins[123]. Nuclear retention of mRNA could diminish protein abundance[124,125]. This differential localization might explain, at least partially, the discrepancy in the mRNA and protein levels of the receptors and contribute to their distinct signaling cascades in cortical circuits. While our HCR-FISH probes were designed to preferentially detect mature, spliced transcripts, we did not perform complementary validation approaches such as oligo-dT FISH, nuclear/cytoplasmic fractionation with RT-qPCR, or metabolic RNA labeling techniques to definitively discriminate between nascent and mature RNA populations[126,127]. However, the differential subcellular localization between *CHRM1* and *CHRM3* remains biologically significant regardless of the specific RNA species detected, as it suggests distinct regulatory mechanisms governing mRNA processing, export, and/or retention.

These mRNA-protein discordance patterns extend to nAChRs, where our snRNAseq data show significant α7 mRNA, but low mRNA expression of α4 and ß2, despite α4β2 nAChRs representing the most abundant subtype by radioligand binding protein measurements[50]. Thus, post-transcriptional and post-translational regulatory mechanisms mentioned above may also be at play for nAChRs. For example, in Alzheimer's disease, protein, but not mRNA expression of the nAChR α4 and α7 subunits is differentially altered, further supporting a role for post-transcriptional regulation[128]. In previous studies in macaque cortex, nAChR radioligand binding protein measurements (e.g., α4 and α2[50]) are not always in line with mRNA expression measured

ARTICLE IN PRESS

ARTICLE IN PRESS

with ISH[49]. Notably, the *CHRM* and *CHRN* expression patterns shown here are comparable to previous snRNAseq studies in macaque and human cortices[51-53], which also show lower detection of these receptor genes relative to their mRNA distribution in the tissue neuropil by ISH[48,49]. These discrepancies in transcript detection between snRNAseq and ISH can be attributed to both transcript localization (somatic versus neuritic) and methodological differences between the approaches. ISH relies on probe-based signal amplification, whereas snRNA-seq uses unique molecular identifier (UMI) counting without amplification and captures only a small fraction of total cellular mRNA, leading to underrepresentation of low-abundance transcripts. Future multiplex FISH and spatial transcriptomics[129] will be important to further understand the nature of transcriptional regulation and trafficking of these receptors within the tissue and cellular compartments.

Our data revealed a high transcriptional similarity between *CHRM1+* and *CHRM3+* ExNs (evidenced by the lack of DEGs), which are distinct from *CHRM2+* ExNs. This similarity reflects the fact that m1 and m3 mAChRs are highly co-expressed and belong to the same M1/M3 pharmacological class, suggesting functional overlap[87]. The M1/M3 class elicits post-synaptic depolarizing effects when bound to ACh, via activation of $G_{q/11}$ proteins and opening of voltage-gated K^+ and Ca^{2+} channels [[87]; reviewed in [10,130,131]]. Indeed, our transcriptional dataset showed *CHRM1/CHRM3+* ExNs display upregulation in genes encoding muscarinic sensitive voltage-gated "M-current" K^+ channels (*KCNQ3*), and R-type high voltage activated Ca^{2+} channels (*CACNA1E)*[132]. M1/M3-activated pathways enhance activity and can trigger downstream spine formation and LTP[9,109,110], consistent with the enrichment of functional terms related to axon guidance, adhesion, and synaptic plasticity in *CHRM1+/CHRM3+* ExNs. In contrast, m2 and m4 receptors belong to the same M2/M4 mAChR pharmacological class that couples to $G_{i/o}$ proteins

ARTICLE IN PRESS

that inhibit adenylyl cyclase, decreasing cAMP and neurotransmitter release[34,37,38] [reviewed in[9,10,130,131]]. Consistent with this, adenylyl cyclase *ADCY1* is downregulated in *CHRM2+* as compared to *CHRM1+ and CHRM3+* ExNs. Furthermore, *CHRM2+* ExNs show upregulation in genes encoding proteins that inhibit glutamate release and action. As such, *GIRK1* encodes an inwardly rectifying K^+ channel that hyperpolarizes neurons to inhibit activity[133], and *GRM3/4* encode mGLUR3/4, metabotropic glutamate receptors linked to presynaptic inhibition of glutamate release[134]. Notably, this predisposition for presynaptic suppression is coupled with enrichment of genes related to synapse formation. In both ACC and LPFC, *CHRM2+* ExNs, were enriched in DEGs coding for positive regulators of synapse maturation *(UNC5D, EPHA5/7, SEMA3A, DCC, TRPC3*)[90,91,96-99,102]. Together, these findings highlight the ability of muscarinic receptors to shape functional connectivity by tuning excitability, synaptic transmission and plasticity.

The particularly high degree of *CHRM1/CHRM3* expression in UL2-3 ExNs and *VIP+*/*CALB2+* InNs shown here suggest that ACh may exert strong excitatory effects on these subpopulations[110,111,135]. In contrast, enrichment of *CHRM2+* in DL5-6 ExNs and *PVALB+* InNs suggest that these subpopulations likely traffic m2 receptors down axons to mediate presynaptic suppression of glutamatergic and GABAergic neurotransmission[34,37,38,40,135,136]. These distinct mAChR expression profiles align with layer-specific ExNs and neurochemical InN subclasses with divergent developmental origins and unique synaptic functions (UL vs. DL ExNs; *VIP/CALB2* caudal vs *PVALB* medial ganglionic eminence InNs[79,137,138]). Indeed, our functional data showed heterogenous effects of ACh on GABAergic neurotransmission, likely reflecting involvement of these diverse neurochemical InN subclasses[40]. Interestingly, InNs expressing the parvalbumin protein (PV+) are more numerous in LPFC than ACC, where other InN subtypes

ARTICLE IN PRESS

predominate[27,139,140]. This regional diversity in cellular composition of InNs may confer diverse regional cholinergic effects on network dynamics of ACC and LPFC.[28,141]

While our snRNA-seq data revealed relatively similar distribution of *CHRM*-enriched cells in ACC and LPFC, the functional effects of mAChRs largely depend on subcellular localization of proteins and cholinergic innervation, which are different between these regions[12,13, 40]. Compared to LPFC, ACC receives denser cholinergic inputs from the basal forebrain[12,13] and exhibits higher density of mAChRs on dendrites of pyramidal ExNs[40]. Compared to LPFC, *CHRM1+/CHRM3+* ExNs in ACC exhibited a significant upregulation of genes that promote synapse formation[90,91,96-99,102], and encode for glutamate receptor subtypes and Ca^{2+} channels that potentiate synaptic responses[104-106]. Similar patterns were observed for *CHRM2+* ExNs, however, there was more pronounced enrichment of terms related to LTD and sodium ion transport than in *CHRM1/3+* ExNs. This is interesting since ACh is a robust modulator of limbic structures, such as the ACC, playing a key role in arousal and memory[3-6]. Further, a subset of DEGs upregulated in ACC relative to LPFC *CHRM2+* ExNs (*SCN9A*, *PRKG1*) are implicated in pain signaling[107,108], a function attributed to the ACC[142,143].

Consistent with our transcriptomic finding of between-region DEGs related to synaptic function and plasticity, our functional profiling revealed regional differences in synaptic properties of L3 pyramidal neurons in response to CCH. Crucially, CCH is a non-selective cholinergic agonist activating both mAChRs and nAChRs[144]. The snRNA-seq analyses revealed that mAChR genes (*CHRM1-3*) show 3-4 fold higher expression than nAChR genes in both ACC and LPFC. These relative expression levels provide a molecular basis for emphasizing mAChR-mediated mechanisms in interpreting our CCH responses. While relative expression does not definitively establish functional dominance, receptor binding studies support the predominance of muscarinic

ARTICLE IN PRESS

ARTICLE IN PRESS

relative to nicotinic ACh receptor activity in macaque cortex[145]. Nonetheless, the α7 subunit (*CHRNA7*), we found to be enriched in a subset of ExN and InN, can enhance glutamate release and may contribute to our observed functional effects[146,147]. Further, rapid desensitization of nAChRs can occur in response to CCH[148] and prolonged exposure to CCH can lead to internalization of m2 mAChRs in neuronal cultures[149,150]. These effects can lead to decreases in responsiveness to CCH across the time-course of exposure. Thus, multi-receptor modulation and dynamic changes in receptor activity across time may contribute to the complexity and heterogeneity of the observed CCH effects and should be examined with receptor-selective pharmacology and time-course experiments in future studies.

Consistent with our previous work[27], CCH amplified inter-areal differences in E:I balance, with ACC neurons exhibiting lower E:I ratios than those in LPFC. In ACC, CCH reduced EPSC and increased IPSC frequency, indicating ACh-mediated presynaptic suppression of excitatory transmission and potentiation of inhibitory transmission, in L3 pyramidal neurons. In contrast, CCH caused no significant changes in EPSC properties in LPFC, but specifically reduced the inhibitory current amplitude, shifting the LPFC microcircuit towards a stronger excitatory tone. Further, while the CCH effect on IPSCs are heterogenous, majority of neurons in ACC showed an increase, but in LPFC showed a decrease in IPSC frequency in response to CCH. At the transcriptomic level, the *CHRM2+* enrichment in *PVALB+* InNs suggest ACh-mediated inhibition at PV+ synapses, while *CHRM1+/3+* enrichment in 'disinhibitory' *CALB2/VIP+* suggest ACh mediated enhancement of activity. These data align with the higher density of PV+ neurons in LPFC that express m2, compared to the predominance of non-PV+ InNs in ACC[40] [27,139,140]. Moreover, these m2+/PV+ terminals are perisomatic-targeting in LPFC, but mainly axo-axonic in

ARTICLE IN PRESS

ACC[40]. The functional impact of these regional differences in m2+/PV+ terminals is unclear and requires future computational and empirical work selectively modulating distinct InN sub-classes.

Previous work in rodents has established a role of ACh in promoting spine structural changes via direct stimulation of microtubule dynamics and neurite outgrowth[102,104-106,112]. The current findings show that cholinergic stimulation via CCH was associated with decreased large mushroom spines and increased thin spines in both ACC and LPFC, suggesting an enhancement of spine motility and weakening of synaptic inputs[151,152]. In ACC neurons, this postsynaptic structural remodeling can be a response to the significant CCH-mediated decrease in presynaptic glutamatergic drive. In LPFC neurons, the magnitude of spine changes is pronounced but CCH excitatory synaptic current suppression was not significant. Thus, our data suggest distinct mechanistic relationships between presynaptic and postsynaptic modulation that may lead to CCH-mediated spine motility in the two areas. This interpretation is supported by our transcriptomic findings where the top enriched genes in ACC *CHRM+* ExNs relative to LPFC are related to spine development and synaptic remodeling pathways (e.g. Roundabout pathway genes, ephrin, cadherins and neuroligins)[90,91,96-99,102]. Interestingly, our washout experiments showed a reversal of CCH-related spine changes in ACC but not in LPFC, which may also be related to the differential enrichment of these plasticity genes.

In contrast to what we have observed here, previous work in rodent cortex has shown that ACh can lead to spine enlargement through via M1/M3 inhibition of K channels, increased excitability and intracellular calcium[111]. However, there is evidence that cholinergic stimulation can also lead to formation of new filopodia and spines, depending on the specific intracellular calcium concertation[151-153]. Thus, given that the LPFC exhibited robust CCH-related structural spine changes without presynaptic current suppression, it is plausible that M1/M3 activation can

ARTICLE IN PRESS

ARTICLE IN PRESS

directly induce a transient increase in intracellular calcium in postsynaptic spines to stimulate downstream intracellular cascades (PKC and MAPK pathways) that regulate actin cytoskeleton dynamics and spine morphology[111,154-156]. This hypothesis is supported by the region-specific upregulation of *CHRM3* and other genes associated to Gq/11 protein signaling in LPFC ExNs. Further, a significant proportion of LPFC pyramidal neurons exhibited a CCH-mediated increase in EPSCs. Given our small sample size of neurons with both spine and synaptic data, our dataset mostly included cells that exhibited a CCH-mediated decrease in EPSCs. Future studies are needed to compare spine changes in neurons with heterogenous EPSC responses to CCH. Further, another important caveat of our study is that the specific mAChR expression profiles of individually recorded neurons were not determined. Future studies employing single-cell transcriptomics from recorded cells[157] would provide more direct mechanistic insights into how specific receptor combinations determine neuronal responses to cholinergic modulation.

Our data revealed that mAChR gene enrichment in ACC and LPFC is associated with between-region transcriptional differences in synapse plasticity pathways that aligned with functional experiments. The relative upregulation of genes promoting synapse plasticity in *CHRM+* ExNs and more pronounced cholinergic suppression of excitatory synaptic currents in ACC, suggests a role of ACh for filtering and enhancing signal-to-noise (gain) of inputs, which can be at play during ACC-mediated tasks requiring high cognitive-emotional demands[7,24,30-32,158,159]. These transcriptional profiles are in line with the critical roles of both the ACC and the cholinergic basal forebrain in emotional regulation, learning and memory[3-7] [reviewed in[8-11]], through their robust interactions with the amygdala[160-163] and hippocampus[164-167]. In rodent prelimbic cortex, a functional analogue of rostral ACC in primates[168,169], ACh has been shown to enhance learning and selectivity of stimuli and responses based on threat and reward valence[170,171]

ARTICLE IN PRESS

[reviewed in [11,166,172]]. On the other hand, *in vivo* assessments in macaque LPFC revealed that muscarinic stimulation can potentiate delayed response activity related to working memory[173]. The cholinergic effect of increased spine plasticity without diminishing excitatory synaptic transmission in LPFC may support flexible maintenance of working memory representations[174-176]. The role of ACh in signal gating and gain modulation has been observed in macaque primary visual cortex[177], rodent prefrontal and olfactory cortices and medial temporal lobe areas [reviewed in[9-11,25]]. A previous ultrastructural study in macaques showed that m2 is preferentially enriched in ACC axons terminating in LPFC[178], implicating ACh in gating reward valence signals from ACC to LPFC, in functions related to cognitive-emotional integration[14-24, 24,27-32] [reviewed in[11,33]]. Our findings support the role of ACh as a modulator of synapse plasticity and E:I circuit dynamics within ACC and LPFC, which can endow flexibility for processing of signals depending on the cholinergic tone and cell-specific activation of distinct muscarinic receptors. Neurochemical ACh imbalance had been long implicated in stress and mood disorders, with more recent work showing rapid anti-depressant effects of the muscarinic antagonist, scopolamine [reviewed in[9, Dulawa, 2019 #209]]. Interestingly, high doses of scopolamine have also been found to disrupt short term and working memory in macaques[174-176]. Our findings suggest that muscarinic block can release m2 presynaptic glutamatergic suppression and 'disinhibit' ACC transmission of signals to LPFC, while dampening activity within LPFC through releasing m2+ suppression of powerful PV+ inhibition and downregulating excitability via blocking M1/M3 receptors. These functional specializations highlight how neuromodulatory systems can sculpt regional circuit properties to support diverse cognitive functions and can lead to pathway-specific disruptions underlying cognitive-emotional impairments in neuropsychiatric disorders.

ARTICLE IN PRESS

References

1 Barbas, H. & Zikopoulos, B. The prefrontal cortex and flexible behavior. *Neuroscientist* **13**, 532-545, doi:10.1177/1073858407301369 (2007).
2 Paus, T. Primate anterior cingulate cortex: where motor control, drive and cognition interface. *Nat Rev Neurosci* **2**, 417-424, doi:10.1038/35077500 (2001).
3 Ballinger, E. C., Ananth, M., Talmage, D. A. & Role, L. W. Basal Forebrain Cholinergic Circuits and Signaling in Cognition and Cognitive Decline. *Neuron* **91**, 1199-1218, doi:10.1016/j.neuron.2016.09.006 (2016).
4 Tikhonova, T. B., Miyamae, T., Gulchina, Y., Lewis, D. A. & Gonzalez-Burgos, G. Cell Type- and Layer-Specific Muscarinic Potentiation of Excitatory Synaptic Drive onto Parvalbumin Neurons in Mouse Prefrontal Cortex. *eNeuro* **5**, doi:10.1523/ENEURO.0208-18.2018 (2018).
5 Obermayer, J., Verhoog, M. B., Luchicchi, A. & Mansvelder, H. D. Cholinergic Modulation of Cortical Microcircuits Is Layer-Specific: Evidence from Rodent, Monkey and Human Brain. *Front Neural Circuits* **11**, 100, doi:10.3389/fncir.2017.00100 (2017).
6 Radnikow, G. & Feldmeyer, D. Layer- and Cell Type-Specific Modulation of Excitatory Neuronal Activity in the Neocortex. *Front Neuroanat* **12**, 1, doi:10.3389/fnana.2018.00001 (2018).
7 Parikh, V., Kozak, R., Martinez, V. & Sarter, M. Prefrontal acetylcholine release controls cue detection on multiple timescales. *Neuron* **56**, 141-154, doi:10.1016/j.neuron.2007.08.025 (2007).
8 Hasselmo, M. E. & Sarter, M. Modes and models of forebrain cholinergic neuromodulation of cognition. *Neuropsychopharmacology* **36**, 52-73, doi:10.1038/npp.2010.104 (2011).
9 Picciotto, M. R., Higley, M. J. & Mineur, Y. S. Acetylcholine as a neuromodulator: cholinergic signaling shapes nervous system function and behavior. *Neuron* **76**, 116-129, doi:10.1016/j.neuron.2012.08.036 (2012).
10 Colangelo, C., Shichkova, P., Keller, D., Markram, H. & Ramaswamy, S. Cellular, Synaptic and Network Effects of Acetylcholine in the Neocortex. *Front Neural Circuits* **13**, 24, doi:10.3389/fncir.2019.00024 (2019).
11 Runyon, K. *et al.* Distinct cholinergic circuits underlie discrete effects of reward on attention. *Front Mol Neurosci* **17**, 1429316, doi:10.3389/fnmol.2024.1429316 (2024).
12 Mash, D. C., White, W. F. & Mesulam, M. M. Distribution of muscarinic receptor subtypes within architectonic subregions of the primate cerebral cortex. *J Comp Neurol* **278**, 265-274, doi:10.1002/cne.902780209 (1988).
13 Ghashghaei, H. T. & Barbas, H. Neural interaction between the basal forebrain and functionally distinct prefrontal cortices in the rhesus monkey. *Neuroscience* **103**, 593-614, doi:10.1016/s0306-4522(00)00585-6 (2001).
14 Johnston, K., Levin, H. M., Koval, M. J. & Everling, S. Top-down control-signal dynamics in anterior cingulate and prefrontal cortex neurons following task switching. *Neuron* **53**, 453-462 (2007).
15 Ito, S., Stuphorn, V., Brown, J. W. & Schall, J. D. Performance monitoring by the anterior cingulate cortex during saccade countermanding. *Science* **302**, 120-122 (2003).
16 MacDonald, A. W., III, Cohen, J. D., Stenger, V. A. & Carter, C. S. Dissociating the role of the dorsolateral prefrontal and anterior cingulate cortex in cognitive control. *Science* **288**, 1835-1838 (2000).

ARTICLE IN PRESS

ARTICLE IN PRESS

17 Botvinick, M. M., Cohen, J. D. & Carter, C. S. Conflict monitoring and anterior cingulate cortex: an update. *Trends Cogn Sci.* **8**, 539-546 (2004).

18 Braver, T. S., Reynolds, J. R. & Donaldson, D. I. Neural mechanisms of transient and sustained cognitive control during task switching. *Neuron* **39**, 713-726 (2003).

19 Brown, J. W. & Braver, T. S. A computational model of risk, conflict, and individual difference effects in the anterior cingulate cortex. *Brain Research* **1202**, 99-108 (2008).

20 Kaping, D., Vinck, M., Hutchison, R. M., Everling, S. & Womelsdorf, T. Specific contributions of ventromedial, anterior cingulate, and lateral prefrontal cortex for attentional selection and stimulus valuation. *PLoS Biol* **9**, e1001224, doi:10.1371/journal.pbio.1001224 (2011).

21 Barbas, H., Saha, S., Rempel-Clower, N. & Ghashghaei, T. Serial pathways from primate prefrontal cortex to autonomic areas may influence emotional expression. *BMC Neuroscience* **4**, 25 (2003).

22 Vogt, B. A. Pain and emotion interactions in subregions of the cingulate gyrus. *Nat.Rev.Neurosci.* **6**, 533-544 (2005).

23 Phelps, E. A. Human emotion and memory: interactions of the amygdala and hippocampal complex. *Current Opinion in Neurobiology* **14**, 198-202 (2004).

24 Voloh, B., Valiante, T. A., Everling, S. & Womelsdorf, T. Theta-gamma coordination between anterior cingulate and prefrontal cortex indexes correct attention shifts. *Proc Natl Acad Sci U S A* **112**, 8457-8462, doi:10.1073/pnas.1500438112 (2015).

25 Hasselmo, M. E. & McGaughy, J. High acetylcholine levels set circuit dynamics for attention and encoding and low acetylcholine levels set dynamics for consolidation. *Prog Brain Res* **145**, 207-231, doi:10.1016/S0079-6123(03)45015-2 (2004).

26 Hasselmo, M. E. & Giocomo, L. M. Cholinergic modulation of cortical function. *J Mol Neurosci* **30**, 133-135, doi:10.1385/JMN:30:1:133 (2006).

27 Medalla, M., Gilman, J. P., Wang, J. Y. & Luebke, J. I. Strength and Diversity of Inhibitory Signaling Differentiates Primate Anterior Cingulate from Lateral Prefrontal Cortex. *J Neurosci* **37**, 4717-4734, doi:10.1523/JNEUROSCI.3757-16.2017 (2017).

28 Medalla, M. *et al.* Layer-specific pyramidal neuron properties underlie diverse anterior cingulate cortical motor and limbic networks. *Cereb Cortex*, doi:10.1093/cercor/bhab347 (2021).

29 Howe, W. M. *et al.* Acetylcholine Release in Prefrontal Cortex Promotes Gamma Oscillations and Theta-Gamma Coupling during Cue Detection. *J Neurosci* **37**, 3215-3230, doi:10.1523/JNEUROSCI.2737-16.2017 (2017).

30 Bernacchia, A., Seo, H., Lee, D. & Wang, X.-J. A reservoir of time constants for memory traces in cortical neurons. *Nature neuroscience* **14**, 366-372, doi:10.1038/nn.2752 (2011).

31 Stoll, F. M., Fontanier, V. & Procyk, E. Specific frontal neural dynamics contribute to decisions to check. *Nature Communications* **7**, 11990, doi:10.1038/ncomms11990 (2016).

32 Newman, L. A. & McGaughy, J. Attentional effects of lesions to the anterior cingulate cortex: how prior reinforcement influences distractibility. *Behav Neurosci* **125**, 360-371, doi:10.1037/a0023250 (2011).

33 Kopell, N., Börgers, C., Pervouchine, D., Malerba, P. & Tort, A. in *Hippocampal Microcircuits: A Computational Modeler's Resource Book* (eds Vassilis Cutsuridis, Bruce Graham, Stuart Cobb, & Imre Vida) 423-457 (Springer New York, 2010).

34 Mrzljak, L., Levey, A. I. & Goldman-Rakic, P. S. Association of m1 and m2 muscarinic receptor proteins with asymmetric synapses in the primate cerebral cortex: morphological

ARTICLE IN PRESS

ARTICLE IN PRESS

evidence for cholinergic modulation of excitatory neurotransmission. *Proc Natl Acad Sci U S A* **90**, 5194-5198, doi:10.1073/pnas.90.11.5194 (1993).

35 Carr, D. B. & Surmeier, D. J. M1 muscarinic receptor modulation of Kir2 channels enhances temporal summation of excitatory synaptic potentials in prefrontal cortex pyramidal neurons. *J Neurophysiol* **97**, 3432-3438, doi:10.1152/jn.00828.2006 (2007).

36 Callender, Julia A. & Newton, Alexandra C. Conventional protein kinase C in the brain: 40 years later. *Neuronal Signaling* **1**, doi:10.1042/ns20160005 (2017).

37 Kimura, F. & Baughman, R. W. Distinct muscarinic receptor subtypes suppress excitatory and inhibitory synaptic responses in cortical neurons. *J Neurophysiol* **77**, 709-716, doi:10.1152/jn.1997.77.2.709 (1997).

38 Salgado, H. *et al.* Muscarinic M2 and M1 receptors reduce GABA release by Ca2+ channel modulation through activation of PI3K/Ca2+ -independent and PLC/Ca2+ -dependent PKC. *J Neurophysiol* **98**, 952-965, doi:10.1152/jn.00060.2007 (2007).

39 Muñoz, W. & Rudy, B. Spatiotemporal specificity in cholinergic control of neocortical function. *Current Opinion in Neurobiology* **26**, 149-160, doi:https://doi.org/10.1016/j.conb.2014.02.015 (2014).

40 Tsolias, A. & Medalla, M. Muscarinic Acetylcholine Receptor Localization on Distinct Excitatory and Inhibitory Neurons Within the ACC and LPFC of the Rhesus Monkey. *Front Neural Circuits* **15**, 795325, doi:10.3389/fncir.2021.795325 (2021).

41 Tsolias, A. *et al.* Neuroanatomical Substrates of Circuit-Specific Cholinergic Modulation across the Primate Anterior Cingulate Cortex. *J Neurosci* **44**, doi:10.1523/JNEUROSCI.0953-23.2024 (2024).

42 Chamling, X. *et al.* Single-cell transcriptomic reveals molecular diversity and developmental heterogeneity of human stem cell-derived oligodendrocyte lineage cells. *Nat Commun* **12**, 652, doi:10.1038/s41467-021-20892-3 (2021).

43 Zhu, Y. *et al.* Spatiotemporal transcriptomic divergence across human and macaque brain development. *Science* **362**, doi:10.1126/science.aat8077 (2018).

44 Li, Z. *et al.* Asynchronous excitatory neuron development in an isogenic cortical spheroid model of Down syndrome. *Front Neurosci* **16**, 932384, doi:10.3389/fnins.2022.932384 (2022).

45 Suresh, H. *et al.* Comparative single-cell transcriptomic analysis of primate brains highlights human-specific regulatory evolution. *Nat Ecol Evol* **7**, 1930-1943, doi:10.1038/s41559-023-02186-7 (2023).

46 Olah, M. *et al.* Single cell RNA sequencing of human microglia uncovers a subset associated with Alzheimer's disease. *Nat Commun* **11**, 6129, doi:10.1038/s41467-020-19737-2 (2020).

47 Flynn, D. D., Ferrari-DiLeo, G., Mash, D. C. & Levey, A. I. Differential regulation of molecular subtypes of muscarinic receptors in Alzheimer's disease. *J Neurochem* **64**, 1888-1891, doi:10.1046/j.1471-4159.1995.64041888.x (1995).

48 Quik, M. *et al.* Localization of nicotinic receptor subunit mRNAs in monkey brain by in situ hybridization. *J Comp Neurol* **425**, 58-69, doi:10.1002/1096-9861(20000911)425:1<58::aid-cne6>3.0.co;2-x (2000).

49 Han, Z. Y. *et al.* Localization of nAChR subunit mRNAs in the brain of Macaca mulatta. *Eur J Neurosci* **12**, 3664-3674, doi:10.1046/j.1460-9568.2000.00262.x (2000).

ARTICLE IN PRESS

ARTICLE IN PRESS

50 Han, Z. Y. *et al.* Localization of [3H]nicotine, [3H]cytisine, [3H]epibatidine, and [125I]alpha-bungarotoxin binding sites in the brain of Macaca mulatta. *J Comp Neurol* **461**, 49-60, doi:10.1002/cne.10659 (2003).

51 Chiou, K. L. *et al.* A single-cell multi-omic atlas spanning the adult rhesus macaque brain. *Sci Adv* **9**, eadh1914, doi:10.1126/sciadv.adh1914 (2023).

52 Jorstad, N. L. *et al.* Transcriptomic cytoarchitecture reveals principles of human neocortex organization. *Science* **382**, eadf6812, doi:10.1126/science.adf6812 (2023).

53 Ma, S. *et al.* Molecular and cellular evolution of the primate dorsolateral prefrontal cortex. *Science* **377**, eabo7257, doi:10.1126/science.abo7257 (2022).

54 Tigges, M., Tigges, J., Rees, H., Rye, D. & Levey, A. I. Distribution of muscarinic cholinergic receptor proteins m1 to m4 in area 17 of normal and monocularly deprived rhesus monkeys. *J Comp Neurol* **388**, 130-145 (1997).

55 Chen, E. Y. *et al.* Enrichr: interactive and collaborative HTML5 gene list enrichment analysis tool. *BMC Bioinformatics* **14**, 128, doi:10.1186/1471-2105-14-128 (2013).

56 Kuleshov, M. V. *et al.* Enrichr: a comprehensive gene set enrichment analysis web server 2016 update. *Nucleic Acids Res* **44**, W90-97, doi:10.1093/nar/gkw377 (2016).

57 Xie, Z. *et al.* Gene Set Knowledge Discovery with Enrichr. *Curr Protoc* **1**, e90, doi:10.1002/cpz1.90 (2021).

58 Craig, A. M. & Kang, Y. Neurexin-neuroligin signaling in synapse development. *Curr Opin Neurobiol* **17**, 43-52, doi:10.1016/j.conb.2007.01.011 (2007).

59 Apperson, M. L., Moon, I. S. & Kennedy, M. B. Characterization of densin-180, a new brain-specific synaptic protein of the O-sialoglycoprotein family. *J Neurosci* **16**, 6839-6852, doi:10.1523/JNEUROSCI.16-21-06839.1996 (1996).

60 Laumonnier, F., Cuthbert, P. C. & Grant, S. G. The role of neuronal complexes in human X-linked brain diseases. *Am J Hum Genet* **80**, 205-220, doi:10.1086/511441 (2007).

61 De Stefano, M. E., Ferretti, V. & Mozzetta, C. Synaptic alterations as a neurodevelopmental trait of Duchenne muscular dystrophy. *Neurobiol Dis* **168**, 105718, doi:10.1016/j.nbd.2022.105718 (2022).

62 Garrett, L. *et al.* Post-synaptic scaffold protein TANC2 in psychiatric and somatic disease risk. *Dis Model Mech* **15**, doi:10.1242/dmm.049205 (2022).

63 Yang, Y. R. *et al.* Primary phospholipase C and brain disorders. *Adv Biol Regul* **61**, 80-85, doi:10.1016/j.jbior.2015.11.003 (2016).

64 Kitazawa, M., Kubo, Y. & Nakajo, K. The stoichiometry and biophysical properties of the Kv4 potassium channel complex with K+ channel-interacting protein (KChIP) subunits are variable, depending on the relative expression level. *J Biol Chem* **289**, 17597-17609, doi:10.1074/jbc.M114.563452 (2014).

65 Skaar, J. R., Pagan, J. K. & Pagano, M. Mechanisms and function of substrate recruitment by F-box proteins. *Nat Rev Mol Cell Biol* **14**, 369-381, doi:10.1038/nrm3582 (2013).

66 Mena, E. L. *et al.* Dimerization quality control ensures neuronal development and survival. *Science* **362**, doi:10.1126/science.aap8236 (2018).

67 Abe, K., Chisaka, O., Van Roy, F. & Takeichi, M. Stability of dendritic spines and synaptic contacts is controlled by alpha N-catenin. *Nat Neurosci* **7**, 357-363, doi:10.1038/nn1212 (2004).

68 Kobielak, A. & Fuchs, E. Alpha-catenin: at the junction of intercellular adhesion and actin dynamics. *Nat Rev Mol Cell Biol* **5**, 614-625, doi:10.1038/nrm1433 (2004).

ARTICLE IN PRESS

ARTICLE IN PRESS

69 Assendorp, N. *et al.* CTNND2 moderates the pace of synaptic maturation and links human evolution to synaptic neoteny. *Cell Rep* **43**, 114797, doi:10.1016/j.celrep.2024.114797 (2024).
70 Formoso, K., Garcia, M. D., Frasch, A. C. & Scorticati, C. Filopodia formation driven by membrane glycoprotein M6a depends on the interaction of its transmembrane domains. *J Neurochem* **134**, 499-512, doi:10.1111/jnc.13153 (2015).
71 Leon, A., Aparicio, G. I. & Scorticati, C. Neuronal Glycoprotein M6a: An Emerging Molecule in Chemical Synapse Formation and Dysfunction. *Front Synaptic Neurosci* **13**, 661681, doi:10.3389/fnsyn.2021.661681 (2021).
72 Lake, B. B. *et al.* Neuronal subtypes and diversity revealed by single-nucleus RNA sequencing of the human brain. *Science* **352**, 1586-1590, doi:10.1126/science.aaf1204 (2016).
73 Zeng, H. *et al.* Large-scale cellular-resolution gene profiling in human neocortex reveals species-specific molecular signatures. *Cell* **149**, 483-496, doi:10.1016/j.cell.2012.02.052 (2012).
74 Tomorsky, J., Parker, P. R. L., Doe, C. Q. & Niell, C. M. Precise levels of nectin-3 are required for proper synapse formation in postnatal visual cortex. *Neural Development* **15**, 13, doi:10.1186/s13064-020-00150-w (2020).
75 Maynard, K. R. *et al.* Transcriptome-scale spatial gene expression in the human dorsolateral prefrontal cortex. *Nat Neurosci* **24**, 425-436, doi:10.1038/s41593-020-00787-0 (2021).
76 Tremblay, R., Lee, S. & Rudy, B. GABAergic Interneurons in the Neocortex: From Cellular Properties to Circuits. *Neuron* **91**, 260-292, doi:10.1016/j.neuron.2016.06.033 (2016).
77 Kawaguchi, Y. & Kubota, Y. GABAergic cell subtypes and their synaptic connections in rat frontal cortex. *Cerebral Cortex* **7**, 476-486 (1997).
78 Markram, H. *et al.* Interneurons of the neocortical inhibitory system. *Nat Rev Neurosci* **5**, 793-807 (2004).
79 Krienen, F. M. *et al.* Innovations present in the primate interneuron repertoire. *Nature* **586**, 262-269, doi:10.1038/s41586-020-2781-z (2020).
80 DeFelipe, J. Types of neurons, synaptic connections and chemical characteristics of cells immunoreactive for calbindin-D28K, parvalbumin and calretinin in the neocortex. *J Chem Neuroanat* **14**, 1-19 (1997).
81 Kanehisa, M., Furumichi, M., Sato, Y., Matsuura, Y. & Ishiguro-Watanabe, M. KEGG: biological systems database as a model of the real world. *Nucleic Acids Res* **53**, D672-D677, doi:10.1093/nar/gkae909 (2025).
82 Kanehisa, M. & Goto, S. KEGG: kyoto encyclopedia of genes and genomes. *Nucleic Acids Res* **28**, 27-30, doi:10.1093/nar/28.1.27 (2000).
83 Ashburner, M. *et al.* Gene ontology: tool for the unification of biology. The Gene Ontology Consortium. *Nat Genet* **25**, 25-29, doi:10.1038/75556 (2000).
84 Gene Ontology, C. *et al.* The Gene Ontology knowledgebase in 2023. *Genetics* **224**, doi:10.1093/genetics/iyad031 (2023).
85 Gantner, C. W. *et al.* FGF-MAPK signaling regulates human deep-layer corticogenesis. *Stem Cell Reports* **16**, 1262-1275, doi:10.1016/j.stemcr.2021.03.014 (2021).
86 Shah, B. *et al.* Rap1 GTPases Are Master Regulators of Neural Cell Polarity in the Developing Neocortex. *Cereb Cortex* **27**, 1253-1269, doi:10.1093/cercor/bhv341 (2017).

ARTICLE IN PRESS

ARTICLE IN PRESS

87 Chen, X. *et al.* Inhibition of a background potassium channel by Gq protein alpha-subunits. *Proc Natl Acad Sci U S A* **103**, 3422-3427, doi:10.1073/pnas.0507710103 (2006).
88 Higashida, H. *et al.* Selective coupling of different muscarinic acetylcholine receptors to neuronal calcium currents in DNA-transfected cells. *Proc Biol Sci* **242**, 68-74, doi:10.1098/rspb.1990.0105 (1990).
89 Gahwiler, B. H. & Brown, D. A. Muscarine affects calcium-currents in rat hippocampal pyramidal cells in vitro. *Neurosci Lett* **76**, 301-306, doi:10.1016/0304-3940(87)90419-8 (1987).
90 Clifford, M. A. *et al.* EphA7 signaling guides cortical dendritic development and spine maturation. *Proc Natl Acad Sci U S A* **111**, 4994-4999, doi:10.1073/pnas.1323793111 (2014).
91 Shelly, M. *et al.* Semaphorin3A regulates neuronal polarization by suppressing axon formation and promoting dendrite growth. *Neuron* **71**, 433-446, doi:10.1016/j.neuron.2011.06.041 (2011).
92 Horn, K. E. *et al.* DCC expression by neurons regulates synaptic plasticity in the adult brain. *Cell Rep* **3**, 173-185, doi:10.1016/j.celrep.2012.12.005 (2013).
93 Hartmann, J., Henning, H. A. & Konnerth, A. mGluR1/TRPC3-mediated Synaptic Transmission and Calcium Signaling in Mammalian Central Neurons. *Cold Spring Harb Perspect Biol* **3**, doi:10.1101/cshperspect.a006726 (2011).
94 Gray, M., Nash, K. R. & Yao, Y. Adenylyl cyclase 2 expression and function in neurological diseases. *CNS Neurosci Ther* **30**, e14880, doi:10.1111/cns.14880 (2024).
95 Szymanowicz, O. *et al.* A Review of the CACNA Gene Family: Its Role in Neurological Disorders. *Diseases* **12**, doi:10.3390/diseases12050090 (2024).
96 Cariboni, A. *et al.* Slit2 and Robo3 modulate the migration of GnRH-secreting neurons. *Development* **139**, 3326-3331, doi:10.1242/dev.079418 (2012).
97 Bisiak, F. & McCarthy, A. A. Structure and Function of Roundabout Receptors. *Subcell Biochem* **93**, 291-319, doi:10.1007/978-3-030-28151-9_9 (2019).
98 Ensslen-Craig, S. E. & Brady-Kalnay, S. M. Receptor protein tyrosine phosphatases regulate neural development and axon guidance. *Dev Biol* **275**, 12-22, doi:10.1016/j.ydbio.2004.08.009 (2004).
99 Emperador-Melero, J. & Kaeser, P. S. Assembly of the presynaptic active zone. *Curr Opin Neurobiol* **63**, 95-103, doi:10.1016/j.conb.2020.03.008 (2020).
100 Mukherjee, A. & Nongthomba, U. To RNA-binding and beyond: Emerging facets of the role of Rbfox proteins in development and disease. *Wiley Interdiscip Rev RNA*, e1813, doi:10.1002/wrna.1813 (2023).
101 Stevanovic, M. *et al.* SOX Transcription Factors as Important Regulators of Neuronal and Glial Differentiation During Nervous System Development and Adult Neurogenesis. *Front Mol Neurosci* **14**, 654031, doi:10.3389/fnmol.2021.654031 (2021).
102 Nabavi, M. & Hiesinger, P. R. Turnover of synaptic adhesion molecules. *Mol Cell Neurosci* **124**, 103816, doi:10.1016/j.mcn.2023.103816 (2023).
103 Cherra, S. J., 3rd & Lamb, R. Interactions between Ras and Rap signaling pathways during neurodevelopment in health and disease. *Front Mol Neurosci* **17**, 1352731, doi:10.3389/fnmol.2024.1352731 (2024).
104 Abraham, W. C., Jones, O. D. & Glanzman, D. L. Is plasticity of synapses the mechanism of long-term memory storage? *NPJ Sci Learn* **4**, 9, doi:10.1038/s41539-019-0048-y (2019).

ARTICLE IN PRESS

ARTICLE IN PRESS

105 Spence, E. F. & Soderling, S. H. Actin Out: Regulation of the Synaptic Cytoskeleton. *J Biol Chem* **290**, 28613-28622, doi:10.1074/jbc.R115.655118 (2015).
106 Malenka, R. C. & Bear, M. F. LTP and LTD: an embarrassment of riches. *Neuron* **44**, 5-21, doi:10.1016/j.neuron.2004.09.012 (2004).
107 Luo, C. *et al.* Presynaptically localized cyclic GMP-dependent protein kinase 1 is a key determinant of spinal synaptic potentiation and pain hypersensitivity. *PLoS Biol* **10**, e1001283, doi:10.1371/journal.pbio.1001283 (2012).
108 Reimann, F. *et al.* Pain perception is altered by a nucleotide polymorphism in SCN9A. *Proc Natl Acad Sci U S A* **107**, 5148-5153, doi:10.1073/pnas.0913181107 (2010).
109 Schatzle, P. *et al.* Rapid and reversible formation of spine head filopodia in response to muscarinic receptor activation in CA1 pyramidal cells. *J Physiol* **589**, 4353-4364, doi:10.1113/jphysiol.2010.204446 (2011).
110 Dennis, S. H. *et al.* Activation of Muscarinic M1 Acetylcholine Receptors Induces Long-Term Potentiation in the Hippocampus. *Cereb Cortex* **26**, 414-426, doi:10.1093/cercor/bhv227 (2016).
111 Giessel, A. J. & Sabatini, B. L. M1 muscarinic receptors boost synaptic potentials and calcium influx in dendritic spines by inhibiting postsynaptic SK channels. *Neuron* **68**, 936-947, doi:10.1016/j.neuron.2010.09.004 (2010).
112 Bourne, J. N. & Harris, K. M. Balancing structure and function at hippocampal dendritic spines. *Annu Rev Neurosci* **31**, 47-67, doi:10.1146/annurev.neuro.31.060407.125646 (2008).
113 Volpicelli, L. A. & Levey, A. I. Muscarinic acetylcholine receptor subtypes in cerebral cortex and hippocampus. *Prog Brain Res* **145**, 59-66, doi:10.1016/S0079-6123(03)45003-6 (2004).
114 Levey, A. I., Edmunds, S. M., Koliatsos, V., Wiley, R. G. & Heilman, C. J. Expression of m1-m4 muscarinic acetylcholine receptor proteins in rat hippocampus and regulation by cholinergic innervation. *J Neurosci* **15**, 4077-4092, doi:10.1523/JNEUROSCI.15-05-04077.1995 (1995).
115 Zilles, K. & Palomero-Gallagher, N. Multiple Transmitter Receptors in Regions and Layers of the Human Cerebral Cortex. *Front Neuroanat* **11**, 78, doi:10.3389/fnana.2017.00078 (2017).
116 Houseley, J. & Tollervey, D. The many pathways of RNA degradation. *Cell* **136**, 763-776, doi:10.1016/j.cell.2009.01.019 (2009).
117 Furlan, M., de Pretis, S. & Pelizzola, M. Dynamics of transcriptional and post-transcriptional regulation. *Brief Bioinform* **22**, doi:10.1093/bib/bbaa389 (2021).
118 Zeisel, A. *et al.* Coupled pre-mRNA and mRNA dynamics unveil operational strategies underlying transcriptional responses to stimuli. *Mol Syst Biol* **7**, 529, doi:10.1038/msb.2011.62 (2011).
119 Luppi, A. I. *et al.* Benchmarking macaque brain gene expression for horizontal and vertical translation. *Sci Adv* **11**, eads6967, doi:10.1126/sciadv.ads6967 (2025).
120 Xu, J. *et al.* Direct SUMOylation of M1 muscarinic acetylcholine receptor increases its ligand-binding affinity and signal transduction. *FASEB J* **33**, 3237-3251, doi:10.1096/fj.201800936R (2019).
121 Romero-Fernandez, W., Borroto-Escuela, D. O., Alea, M. P., Garcia-Mesa, Y. & Garriga, P. Altered trafficking and unfolded protein response induction as a result of M3 muscarinic

ARTICLE IN PRESS

ARTICLE IN PRESS

receptor impaired N-glycosylation. *Glycobiology* **21**, 1663-1672, doi:10.1093/glycob/cwr105 (2011).
122 Patwardhan, A., Cheng, N. & Trejo, J. Post-Translational Modifications of G Protein-Coupled Receptors Control Cellular Signaling Dynamics in Space and Time. *Pharmacol Rev* **73**, 120-151, doi:10.1124/pharmrev.120.000082 (2021).
123 Gilbertson, S., Federspiel, J. D., Hartenian, E., Cristea, I. M. & Glaunsinger, B. Changes in mRNA abundance drive shuttling of RNA binding proteins, linking cytoplasmic RNA degradation to transcription. *Elife* **7**, doi:10.7554/eLife.37663 (2018).
124 Bahar Halpern, K. *et al.* Nuclear Retention of mRNA in Mammalian Tissues. *Cell Rep* **13**, 2653-2662, doi:10.1016/j.celrep.2015.11.036 (2015).
125 Steinbrecht, D. *et al.* Subcellular mRNA kinetic modeling reveals nuclear retention as rate-limiting. *Mol Syst Biol* **20**, 1346-1371, doi:10.1038/s44320-024-00073-2 (2024).
126 Solnestam, B. W. *et al.* Comparison of total and cytoplasmic mRNA reveals global regulation by nuclear retention and miRNAs. *BMC Genomics* **13**, 574, doi:10.1186/1471-2164-13-574 (2012).
127 Tsai, Y. L., Mu, Y. C. & Manley, J. L. Nuclear RNA transcript levels modulate nucleocytoplasmic distribution of ALS/FTD-associated protein FUS. *Sci Rep* **12**, 8180, doi:10.1038/s41598-022-12098-4 (2022).
128 Wevers, A. *et al.* Expression of nicotinic acetylcholine receptors in Alzheimer's disease: postmortem investigations and experimental approaches. *Behav Brain Res* **113**, 207-215, doi:10.1016/s0166-4328(00)00215-1 (2000).
129 Yue, L. *et al.* A guidebook of spatial transcriptomic technologies, data resources and analysis approaches. *Comput Struct Biotechnol J* **21**, 940-955, doi:10.1016/j.csbj.2023.01.016 (2023).
130 Groleau, M., Kang, J. I., Huppe-Gourgues, F. & Vaucher, E. Distribution and effects of the muscarinic receptor subtypes in the primary visual cortex. *Front Synaptic Neurosci* **7**, 10, doi:10.3389/fnsyn.2015.00010 (2015).
131 Brown, D. A. Regulation of neural ion channels by muscarinic receptors. *Neuropharmacology* **136**, 383-400, doi:10.1016/j.neuropharm.2017.11.024 (2018).
132 Wormuth, C. *et al.* Review: Ca(v)2.3 R-type Voltage-Gated Ca(2+) Channels - Functional Implications in Convulsive and Non-convulsive Seizure Activity. *Open Neurol J* **10**, 99-126, doi:10.2174/1874205X01610010099 (2016).
133 Luscher, C., Jan, L. Y., Stoffel, M., Malenka, R. C. & Nicoll, R. A. G protein-coupled inwardly rectifying K+ channels (GIRKs) mediate postsynaptic but not presynaptic transmitter actions in hippocampal neurons. *Neuron* **19**, 687-695, doi:10.1016/s0896-6273(00)80381-5 (1997).
134 Upreti, C., Zhang, X. L., Alford, S. & Stanton, P. K. Role of presynaptic metabotropic glutamate receptors in the induction of long-term synaptic plasticity of vesicular release. *Neuropharmacology* **66**, 31-39, doi:10.1016/j.neuropharm.2012.05.004 (2013).
135 Gigout, S. *et al.* Distinct muscarinic acetylcholine receptor subtypes mediate pre- and postsynaptic effects in rat neocortex. *BMC Neurosci* **13**, 42, doi:10.1186/1471-2202-13-42 (2012).
136 Wang, L. & Yuan, L. L. Activation of M2 muscarinic receptors leads to sustained suppression of hippocampal transmission in the medial prefrontal cortex. *J Physiol* **587**, 5139-5147, doi:10.1113/jphysiol.2009.174821 (2009).

ARTICLE IN PRESS

ARTICLE IN PRESS

137 Miyoshi, G. *et al.* Genetic fate mapping reveals that the caudal ganglionic eminence produces a large and diverse population of superficial cortical interneurons. *J Neurosci* **30**, 1582-1594, doi:10.1523/JNEUROSCI.4515-09.2010 (2010).

138 Ma, T. *et al.* Subcortical origins of human and monkey neocortical interneurons. *Nat Neurosci* **16**, 1588-1597, doi:10.1038/nn.3536 (2013).

139 Dombrowski, S. M., Hilgetag, C. C. & Barbas, H. Quantitative architecture distinguishes prefrontal cortical systems in the rhesus monkey. *Cereb Cortex* **11**, 975-988, doi:10.1093/cercor/11.10.975 (2001).

140 Gabbott, P. L. & Bacon, S. J. Local circuit neurons in the medial prefrontal cortex (areas 24a,b,c, 25 and 32) in the monkey: I. Cell morphology and morphometrics. *J Comp Neurol* **364**, 567-608, doi:10.1002/(SICI)1096-9861(19960122)364:4<567::AID-CNE1>3.0.CO;2-1 (1996).

141 Buzsáki, G., Kaila, K. & Raichle, M. Inhibition and Brain Work. *Neuron* **56**, 771-783, doi:https://doi.org/10.1016/j.neuron.2007.11.008 (2007).

142 Vogt, B. A. & Sikes, R. W. The medial pain system, cingulate cortex, and parallel processing of nociceptive information. *Prog Brain Res* **122**, 223-235, doi:10.1016/s0079-6123(08)62141-x (2000).

143 Fuchs, P. N., Peng, Y. B., Boyette-Davis, J. A. & Uhelski, M. L. The anterior cingulate cortex and pain processing. *Front Integr Neurosci* **8**, 35, doi:10.3389/fnint.2014.00035 (2014).

144 Lucas-Meunier, E. *et al.* Involvement of nicotinic and muscarinic receptors in the endogenous cholinergic modulation of the balance between excitation and inhibition in the young rat visual cortex. *Cereb Cortex* **19**, 2411-2427, doi:10.1093/cercor/bhn258 (2009).

145 Zilles, K., Palomero-Gallagher, N. & Schleicher, A. Transmitter receptors and functional anatomy of the cerebral cortex. *Journal of anatomy* **205**, 417-432, doi:10.1111/j.0021-8782.2004.00357.x (2004).

146 Lozada, A. F. *et al.* Glutamatergic synapse formation is promoted by alpha7-containing nicotinic acetylcholine receptors. *J Neurosci* **32**, 7651-7661, doi:10.1523/JNEUROSCI.6246-11.2012 (2012).

147 McGehee, D. S., Heath, M. J., Gelber, S., Devay, P. & Role, L. W. Nicotine enhancement of fast excitatory synaptic transmission in CNS by presynaptic receptors. *Science* **269**, 1692-1696, doi:10.1126/science.7569895 (1995).

148 Quick, M. W. & Lester, R. A. Desensitization of neuronal nicotinic receptors. *J Neurobiol* **53**, 457-478, doi:10.1002/neu.10109 (2002).

149 Lambert, L. *et al.* Endocytosis of Activated Muscarinic m2 Receptor (m2R) in Live Mouse Hippocampal Neurons Occurs via a Clathrin-Dependent Pathway. *Front Cell Neurosci* **12**, 450, doi:10.3389/fncel.2018.00450 (2018).

150 Wan, M. *et al.* Unraveling a molecular determinant for clathrin-independent internalization of the M2 muscarinic acetylcholine receptor. *Sci Rep* **5**, 11408, doi:10.1038/srep11408 (2015).

151 Henley, J. & Poo, M. M. Guiding neuronal growth cones using Ca2+ signals. *Trends Cell Biol* **14**, 320-330, doi:10.1016/j.tcb.2004.04.006 (2004).

152 Holcman, D., Schuss, Z. & Korkotian, E. Calcium dynamics in dendritic spines and spine motility. *Biophys J* **87**, 81-91, doi:10.1529/biophysj.103.035972 (2004).

153 Zheng, J. Q. & Poo, M. M. Calcium signaling in neuronal motility. *Annu Rev Cell Dev Biol* **23**, 375-404, doi:10.1146/annurev.cellbio.23.090506.123221 (2007).

ARTICLE IN PRESS

ARTICLE IN PRESS

154 Okamoto, K., Narayanan, R., Lee, S. H., Murata, K. & Hayashi, Y. The role of CaMKII as an F-actin-bundling protein crucial for maintenance of dendritic spine structure. *Proc Natl Acad Sci U S A* **104**, 6418-6423, doi:10.1073/pnas.0701656104 (2007).

155 Wotta, D. R., Wattenberg, E. V., Langason, R. B. & el-Fakahany, E. E. M1, M3 and M5 muscarinic receptors stimulate mitogen-activated protein kinase. *Pharmacology* **56**, 175-186, doi:10.1159/000028196 (1998).

156 Oertner, T. G. & Matus, A. Calcium regulation of actin dynamics in dendritic spines. *Cell Calcium* **37**, 477-482, doi:10.1016/j.ceca.2005.01.016 (2005).

157 Cadwell, C. R. *et al.* Electrophysiological, transcriptomic and morphologic profiling of single neurons using Patch-seq. *Nat Biotechnol* **34**, 199-203, doi:10.1038/nbt.3445 (2016).

158 Botvinick, M. M., Braver, T. S., Barch, D. M., Carter, C. S. & Cohen, J. D. Conflict monitoring and cognitive control. *Psychol Rev* **108**, 624-652, doi:10.1037/0033-295x.108.3.624 (2001).

159 Stokes, Mark G. *et al.* Dynamic Coding for Cognitive Control in Prefrontal Cortex. *Neuron* **78**, 364-375, doi:https://doi.org/10.1016/j.neuron.2013.01.039 (2013).

160 Barbas, H., Saha, S., Rempel-Clower, N. & Ghashghaei, T. Serial pathways from primate prefrontal cortex to autonomic areas may influence emotional expression. *BMC Neurosci* **4**, 25, doi:10.1186/1471-2202-4-25 (2003).

161 Calderazzo, S. M., Busch, S. E., Moore, T. L., Rosene, D. L. & Medalla, M. Distribution and overlap of entorhinal, premotor, and amygdalar connections in the monkey anterior cingulate cortex. *J Comp Neurol* **529**, 885-904, doi:10.1002/cne.24986 (2021).

162 Kim, Y. *et al.* Afferent connections of the dorsal, perigenual, and subgenual anterior cingulate cortices of the monkey: Amygdalar inputs and intrinsic connections. *Neurosci Lett* **681**, 93-99, doi:10.1016/j.neulet.2018.05.028 (2018).

163 Sharma, K. K., Kelly, E. A., Pfeifer, C. W. & Fudge, J. L. Translating Fear Circuitry: Amygdala Projections to Subgenual and Perigenual Anterior Cingulate in the Macaque. *Cereb Cortex* **30**, 550-562, doi:10.1093/cercor/bhz106 (2020).

164 Anderson, M. C., Bunce, J. G. & Barbas, H. Prefrontal-hippocampal pathways underlying inhibitory control over memory. *Neurobiol Learn Mem* **134 Pt A**, 145-161, doi:10.1016/j.nlm.2015.11.008 (2016).

165 Wang, J., John, Y. & Barbas, H. Pathways for Contextual Memory: The Primate Hippocampal Pathway to Anterior Cingulate Cortex. *Cereb Cortex* **31**, 1807-1826, doi:10.1093/cercor/bhaa333 (2021).

166 Aggleton, J. P., Wright, N. F., Rosene, D. L. & Saunders, R. C. Complementary Patterns of Direct Amygdala and Hippocampal Projections to the Macaque Prefrontal Cortex. *Cereb Cortex* **25**, 4351-4373, doi:10.1093/cercor/bhv019 (2015).

167 Insausti, R. & Munoz, M. Cortical projections of the non-entorhinal hippocampal formation in the cynomolgus monkey (Macaca fascicularis). *Eur J Neurosci* **14**, 435-451, doi:10.1046/j.0953-816x.2001.01662.x (2001).

168 Schaeffer, D. J. *et al.* Divergence of rodent and primate medial frontal cortex functional connectivity. *Proc Natl Acad Sci U S A* **117**, 21681-21689, doi:10.1073/pnas.2003181117 (2020).

169 Walton, M. E., Bannerman, D. M., Alterescu, K. & Rushworth, M. F. Functional specialization within medial frontal cortex of the anterior cingulate for evaluating effort-related decisions. *J Neurosci* **23**, 6475-6479, doi:10.1523/JNEUROSCI.23-16-06475.2003 (2003).

ARTICLE IN PRESS

ARTICLE IN PRESS

170 Tu, G., Wen, P., Halawa, A. & Takehara-Nishiuchi, K. Acetylcholine modulates prefrontal outcome coding during threat learning under uncertainty. *Elife* **13**, doi:10.7554/eLife.102986 (2025).

171 Liu, W. Z. *et al.* Identification of a prefrontal cortex-to-amygdala pathway for chronic stress-induced anxiety. *Nat Commun* **11**, 2221, doi:10.1038/s41467-020-15920-7 (2020).

172 McGaughy, J., Everitt, B. J., Robbins, T. W. & Sarter, M. The role of cortical cholinergic afferent projections in cognition: impact of new selective immunotoxins. *Behav Brain Res* **115**, 251-263, doi:10.1016/s0166-4328(00)00262-x (2000).

173 Galvin, V. C. *et al.* Muscarinic M1 Receptors Modulate Working Memory Performance and Activity via KCNQ Potassium Channels in the Primate Prefrontal Cortex. *Neuron* **106**, 649-661 e644, doi:10.1016/j.neuron.2020.02.030 (2020).

174 Vijayraghavan, S., Major, A. J. & Everling, S. Muscarinic M1 Receptor Overstimulation Disrupts Working Memory Activity for Rules in Primate Prefrontal Cortex. *Neuron* **98**, 1256-1268 e1254, doi:10.1016/j.neuron.2018.05.027 (2018).

175 Bartus, R. T. & Johnson, H. R. Short-term memory in the rhesus monkey: disruption from the anti-cholinergic scopolamine. *Pharmacol Biochem Behav* **5**, 39-46, doi:10.1016/0091-3057(76)90286-0 (1976).

176 Croxson, P. L., Kyriazis, D. A. & Baxter, M. G. Cholinergic modulation of a specific memory function of prefrontal cortex. *Nat Neurosci* **14**, 1510-1512, doi:10.1038/nn.2971 (2011).

177 Disney, A. A., Aoki, C. & Hawken, M. J. Gain modulation by nicotine in macaque v1. *Neuron* **56**, 701-713, doi:10.1016/j.neuron.2007.09.034 (2007).

178 Medalla, M. & Barbas, H. The anterior cingulate cortex may enhance inhibition of lateral prefrontal cortex via m2 cholinergic receptors at dual synaptic sites. *J Neurosci* **32**, 15611-15625, doi:10.1523/JNEUROSCI.2339-12.2012 (2012).

179 Amatrudo, J. M. *et al.* Influence of highly distinctive structural properties on the excitability of pyramidal neurons in monkey visual and prefrontal cortices. *J Neurosci* **32**, 13644-13660, doi:10.1523/JNEUROSCI.2581-12.2012 (2012).

180 Barbas, H. & Pandya, D. N. Architecture and intrinsic connections of the prefrontal cortex in the rhesus monkey. *J Comp Neurol* **286**, 353-375, doi:10.1002/cne.902860306 (1989).

181 Morecraft, R. J. *et al.* Cytoarchitecture and cortical connections of the anterior cingulate and adjacent somatomotor fields in the rhesus monkey. *Brain Res Bull* **87**, 457-497, doi:10.1016/j.brainresbull.2011.12.005 (2012).

182 Petrides, M. & Pandya, D. N. Dorsolateral prefrontal cortex: comparative cytoarchitectonic analysis in the human and the macaque brain and corticocortical connection patterns. *Eur J Neurosci* **11**, 1011-1036, doi:10.1046/j.1460-9568.1999.00518.x (1999).

183 Krishnaswami, S. R. *et al.* Using single nuclei for RNA-seq to capture the transcriptome of postmortem neurons. *Nat Protoc* **11**, 499-524, doi:10.1038/nprot.2016.015 (2016).

184 Zheng, G. X. *et al.* Massively parallel digital transcriptional profiling of single cells. *Nat Commun* **8**, 14049, doi:10.1038/ncomms14049 (2017).

185 Butler, A., Hoffman, P., Smibert, P., Papalexi, E. & Satija, R. Integrating single-cell transcriptomic data across different conditions, technologies, and species. *Nat Biotechnol* **36**, 411-420, doi:10.1038/nbt.4096 (2018).

186 Jenkins, D. F. F., T.; Briars, E.; Carrasco, S.; Cunningham, S.; Campbell, J.D D.; Yajima, M.; Johnson W. E. (bioRxiv 329755 2018).

ARTICLE IN PRESS

ARTICLE IN PRESS

187 Choi, H. M. T. *et al.* Third-generation in situ hybridization chain reaction: multiplexed, quantitative, sensitive, versatile, robust. *Development* **145**, doi:10.1242/dev.165753 (2018).
188 Schwarzkopf, M. *et al.* Hybridization chain reaction enables a unified approach to multiplexed, quantitative, high-resolution immunohistochemistry and in situ hybridization. *Development* **148**, doi:10.1242/dev.199847 (2021).
189 Bankhead, P. *et al.* QuPath: Open source software for digital pathology image analysis. *Sci Rep* **7**, 16878, doi:10.1038/s41598-017-17204-5 (2017).
190 Ting, J. T. *et al.* Preparation of Acute Brain Slices Using an Optimized N-Methyl-D-glucamine Protective Recovery Method. *J Vis Exp*, doi:10.3791/53825 (2018).
191 Medalla, M. & Luebke, J. I. Diversity of glutamatergic synaptic strength in lateral prefrontal versus primary visual cortices in the rhesus monkey. *J Neurosci* **35**, 112-127, doi:10.1523/JNEUROSCI.3426-14.2015 (2015).

ARTICLE IN PRESS

ARTICLE IN PRESS

Materials & Methods

Experimental subjects. Brain tissues used in this study were from 14 adult rhesus monkeys (*Macaca mulatta*) of both sexes that were subjects in larger studies of brain aging and cognition (R01/RF1AG068168 and RF1AG043640; n=10 males, ages 7.5-24.8 y and n =4 females ages 8.4-10.4 y; Supplementary Table 1). Monkeys were obtained from either National Primate Centers or private vendors with complete health records. All monkeys were received medical examinations and were subject to magnetic resonance imaging (MRI) of the brain for parallel studies and to ensure absence of any neurological damage. Monkeys with a history of any chronic illness and neurological diseases were excluded from the study. Monkeys were individually housed, under a 12-h light/dark cycle in the Laboratory Animal Science Center (LASC) at Chobanian and Avedisian Boston University School of Medicine. The monkeys were provided some enrichment and were in constant auditory and visual range of other monkeys. They were checked daily by trained observers for health and well-being and were given a medical exam every 3 months by a Clinical Veterinarian at BU LASC. The BU LASC is fully accredited by the Association for Assessment and Accreditation of Laboratory Animal Care. All animal research was conducted in strict accordance with guidelines of the National Institutes of Health's *Guide for the Care and Use of Laboratory Animals* and the *U.S. Public Health Service Policy on Humane Care* and the Boston University Institutional Animal Care and Use Committee. We have complied with all relevant ethical regulations for animal use.

Tissue collection for acute slice preparation and molecular experiments. Tissue was harvested using a two-stage transcardial perfusion protocol that allowed for the harvest of live tissue prior to completing the perfusion fixation of the remaining brain tissue[179]. The animals were initially

ARTICLE IN PRESS

ARTICLE IN PRESS

sedated with ketamine hydrochloride (10 mg/kg) and deeply anesthetized with sodium pentobarbital (to effect, 15 mg/kg, i.v) or propofol (to effect, 0.4 mg/kg/min, i.v.), followed by a two-stage transcardial perfusion that begins with ice-cold (4°C) Krebs–Henseleit buffer to clear the vasculature and slow proteolysis to allow for the harvest of fresh tissue from the left hemisphere for molecular and electrophysiological experiments. The first block of tissue (~10 mm^3) was extracted from the LPFC, within the caudal half of area 46 (A46) to include the dorsal and ventral banks of the principal sulcus[180]. The second block of the same size (~10 mm^3) was removed from the ACC, to include area A24b and A24c in ventral bank of the cingulate sulcus, extending to the cingulate gyrus[180,181] (Fig. 1A). Each block was transferred into oxygenated (95% O_2, 5% CO_2) ice-cold Ringer's solution (in mM: 26 $NaHCO_3$, 124 NaCl, 2 KCl, 3 KH_2PO_4, 10 glucose, and 1.3 $MgCl_2$, pH 7.4), and trimmed into two pieces as follows: one piece (caudal part of ACC A24 and dorsal LPFC A46 in the dorsal bank of the principal sulcus) was flash frozen in liquid nitrogen and stored at -80°C for single nucleus RNA sequencing experiments; and a second piece (rostral part of ACC A24 and ventral LPFC A46) was vibratome-sectioned into 300 µm acute slices for electrophysiological recordings. Based on previous maps of regions in the macaque brain, our gross sampling ensured we are well within the cytoarchitectonic boundaries of A46[182]. However, we acknowledge that our A24 ACC block contain cells from two distinct A24 cytoarchitectonic subareas, 24b and 24c, which we cannot distinguish in snRNAseq dataset. Upon completion of the tissue harvest, the perfusate was switched to 4% paraformaldehyde in 0.1M phosphate buffer (PB, pH 7.4, 37°C) to fix the remaining brain tissue. The brain was then carefully removed, weighed, and post-fixed in 4% paraformaldehyde prior to being cryoprotected through a series of glycerol solution. The brains were ultimately flash-frozen in -70°C isopentane (Rosene et al., 1986) and

ARTICLE IN PRESS

ARTICLE IN PRESS

stored at -80ºC until they are cut on a freezing microtome in the coronal plane at 30 and/or 60µm sections and stored in 15% glycerol buffer for tissue analysis.

Processing brain tissue samples for single nucleus RNA sequencing (snRNA-seq). ACC and LPFC tissue samples that were previously flash-frozen and stored at -80ºC were dissociated by Dounce homogenization in lysis buffer (250mM sucrose, 25mM KCl, 5mM $MgCl_2$, 10mM Tris buffer, pH 8.0, 0.1% Triton X-100, 1µM DTT, 1x Protease inhibitor, 1x RNase inhibitor and 1µM DAPI). The homogenate was then filtered through a 40-µm cell strainer to collect single nuclei. Fluorescence-activated cell-sorting (FACS) was performed at the Chobanian and Avedisian BUSOM Flow Cytometry Core Facility on the BD FACS ARIA II SORP (Becton Dickson) to remove cellular debris and to capture singlets by gating on forward and side-scatter light properties and nuclei fluorescent expression of DAPI. We collected 50,000 nuclei into a collection buffer (0.04% Bovine Serum Albumin (BSA), in PBS supplemented with 1x Protease inhibitor, and 1x RNase inhibitor) as previously described[183].

The sorted nuclei were then processed at the Chobanian and Avedisian BUSOM Microarray and Sequencing Resource Core Facility using the Chromium droplet-based platform (10X Genomics) whereby single nuclei, reagents, and a single gel bead containing barcoded oligonucleotides are encapsulated into nanoliter-sized Gel Bead-in-Emulsion (GEMs) using the GemCode platform for downstream reverse transcription of RNAs. Full length, barcoded cDNA was then amplified by polymerase chain reaction (PCR) for the generation of snRNA-seq libraries. The resulting cDNA libraries were assessed via Bioanalyzer High Sensitivity DNA Assay (Agilent Technologies, USA) and sequences on an Illumina NextSeq500 instrument with the target capture of 2000 cells per sample in accordance with the Illumina and 10x Genomics guidelines with 1.4-18.8 input and 1% PhiX control library spike-in (Illumina, USA).

ARTICLE IN PRESS

ARTICLE IN PRESS

snRNA-seq processing and analyses. The sequencing reads were processed with the 10X Genomics Cell Ranger V3 pipeline[184] using a modified reference that included both introns and exons regions to generate a unique molecular identifier (UMI)/feature-barcode matrix. Quality control was performed using Seurat[185] (RRID:SCR_016341) and singleCellTK[186] (RRID:SCR_026813) packages in R software (RRID:SCR_001905; Supplementary Fig. 1A-D). Nuclei were excluded based on lower numbers of UMIs detected (≤200) or high percentage of counts derived from mitochondrial genes (≥7.5%). Features that were detected in fewer than 3 cells were excluded. The Seurat package was also used for clustering while normalization was performed with the NormalizeData function. Variable features were selected with the FindVariableFeatures function using the "vst" method. Principal component analysis (PCA) was performed using the top 2,000 most variable genes with the RunPCA function. Clustering of cells was implemented with the FindClusters function using 35 PCs. Cell types were annotated based on canonical markers[42-46] (Supplementary Table 2; Supplementary Fig. 1). For more granular analyses, re-clustering of cell types annotated as ExN or InNs was performed to identify subclusters and annotate them based on canonical layer-specific ExN and neurochemical InN markers from the literature[42-46] (Supplementary Table 2; Supplementary Fig. 2).

For further validation of tissue dissection, we determined region-specific markers enriched in ACC vs LPFC ExNs and InNs (Supplementary Data 1) as follows: First, differentially expressed genes (DEGs) between ACC and LPFC were identified within ExN and InN subpopulations, using Seurat's FindMarkers function (Wilcoxon test; logfc.threshold = 0.1, min.pct = 0.2). Genes were retained if they had an FDR < 0.05 (Benjamini–Hochberg correction). The top 10 ACC- and LPFC-enriched genes per neuronal class were visualized using Seurat's DotPlot, with dot size denoting expression frequency and color intensity indicating mean expression.

ARTICLE IN PRESS

It is also important to note that our snRNAseq dataset includes only male monkeys that vary in age. In UMAPs and enrichment bar plots showing distribution of nuclei based on subject, age, and area, we found a representation of nuclei from young and aged monkeys and from each case and area, within each cell cluster (Supplementary Fig. 1D). We also conducted some analyses to assess between-age differences in our markers of interest and specifically found largely no correlations between age and the number of *CHRM*-expressing cells and mean expression levels of *CHRM1-4*. There was however a specific difference in LPFC ExNs, where *CHRM3* expression level was significantly greater in young compared to aged (Log2FC = 2.01e-08, adjusted $p < 0.0004$). Studies with larger sample size are underway and will assess the effect of sex and age on these expression profiles.

The enrichment of RNA expression of markers of interest (*CHRM1*, *CHRM2*, *CHRM*3, *CHRM4*) among the major cell type clusters and among each layer-specific ExN and neurochemically-distinct InN subcluster in ACC and LPFC was calculated based of the proportion of cells expressing these genes. Within total and each sub-cluster of excitatory (ExN) and inhibitory (InN) neurons, differentially expressed genes (DEGs) between pairs of distinct *CHRM1-4* subpopulations and between ACC and LPFC regions were assessed using Seurat's FindMarkers function. Lastly, using the list of DEGs from each comparison, we performed a gene-ontology (GO) analysis using a gene set search engine EnrichR (https://maayanlab.cloud/Enrichr/; RRID:SCR_001575)[55]. Post-analysis filtering was used to cutoff at an adjusted p-value of $p < 0.05$ and a |Log2FC| threshold > 0.25.

Immunohistochemistry and HCR-FISH. To validate our snRNA-seq data, we performed combined immunohistochemical (IHC) and fluorescent in situ hybridization (FISH) using hybridization chain reaction (HCR)[187,188] on serial coronal sections of archived tissue from 4

ARTICLE IN PRESS

monkeys (Supplementary Table 3). Prior to IHC-FISH experiments, frozen 30-µm tissue sections were post-fixed in 4% PFA for 2 hrs at RT. Sections were then rinsed (3 x 10 min, RT) in 0.01M RNase-free phosphate-buffered saline (PBS; Gibco) and stored in filtered 70% RNase-free, molecular grade ethanol in 4ºC until use. IHC was performed to visualize and quantify the expression of m1 and m3 cholinergic receptor proteins, as previously described[40,41]. Briefly, sections were incubated in 50mM glycine in 0.01 M PBS, pH 7.4, to quench free aldehydes from the fixation step. The sections were then rinsed in 0.01 M PBS (3 x 10 min, RT) and incubated in 10 mM sodium citrate, pH 8.5, in a 70ºC water bath for 20 min for antigen retrieval. After rinsing in 0.01 M PBS (3 x 10 min, RT), the sections were incubated in a blocking solution [0.01M PBS, 5% bovine serum albumin (BSA), 5% normal donkey serum (NDS), 0.2% Triton X-100] to reduce non-specific binding of secondary antibodies. Sections were then incubated with gentle agitation at 4ºC for 48 hr in a solution with primary antibodies against MAP2, m1, and m3 receptors [diluted in 0.1M PB, 0.2% acetylated BSA (BSA-c, Aurion), 1 % NDS, 0.1 % Triton X-100; Supplementary Table 3]. To enhance antibody penetration, sections were microwaved for two sessions (2 x 10 min, 150W, 37ºC per session) in low-wattage PELCO Biowave (Ted Pella Inc.). After incubation with primary antibodies, the sections were rinsed in 0.01 M PBS (3 x 10 min, RT), were microwaved for a single session (2 x 10 min, 150W, 37ºC), and were incubated with gentle agitation at 4ºC overnight in a solution with secondary antibodies (Supplementary Table 3). Prior to HCR-FISH, sections were rinsed (3 x 10 min, RT) in 0.01M PBS, post-fixed with 4% PFA for 30 min at RT, and dehydrated with 70% ethanol for 30 min at 4ºC. Afterward, sections were rinsed in 2x Ultrapure saline sodium citrate (SSC, ThermoFisher Scientific) buffer (3 x 1 hr, RT). Sections were then equilibrated with Hybridization Buffer (Molecular Instruments) for 30 min at 37ºC before overnight hybridization with HCR Probes for *CHRM1* and *CHRM3* (final

ARTICLE IN PRESS

ARTICLE IN PRESS

concentration of 4 nM, Supplementary Table 3) in Hybridization Buffer at 37°C. The HCR Probes were designed by Molecular Instruments to span multiple exon-exon junctions and therefore recognize mature, spliced transcripts. Control experiments were run in parallel with HCR probes against the U6 small nuclear RNA (*RNU6*) and poly(A) as positive controls, and the bacterial enzyme dihydrodipicolinate reductase (*dapB*) as negative control (Supplementary Fig. 1P). The next day, sections were rinsed with Probe Wash Buffer (3 x 10 min and 1 x 1 hr, 37°C) and with 5x SSC with Tween-20 (SSCT) (3 x 5 min, RT). Afterward, the sections were equilibrated with Amplification Buffer (Molecular Instruments) for 30 min at 37°C. During the equilibration step, fluorescently labeled HCR hairpins were denatured at 95°C for 90 sec and then cooled to RT for 30 min. The denatured hairpins (final concentration of 60 nM) were combined into a new tube with Amplification Buffer and applied to tissue sections for 16 hrs in the dark at RT. The following day, the sections were rinsed with 5x SSCT (3 x 5 min and 1 x 30 min, 4°C) before an overnight incubation at 4°C with fresh 5x SSCT. Sections were then mounted onto Superfrost Plus glass slides (Fisher Scientific), coverslipped with ProLong Gold Antifade Mountant (Thermo Fisher Scientific), and cured at RT in the dark. Antibody specificity has been validated my manufacturers (see Supplementary Table 3), except for the goat anti-m1 polyclonal antibody (Abcam, ab77098; RRID AB_1523990). To assess the specificity of this anti-m1 receptor antibody in rhesus macaque tissue, we performed a preadsorption control. Because the specific immunogen sequence for this antibody is proprietary and a blocking peptide was unavailable, we performed a preadsorption control using full-length recombinant m1 receptor protein (Novus H00001128-G01). We first incubated the primary antibody together with the m1 receptor protein (1:5) overnight at 4°C, and then incubated tissue sections with preabsorbed m1 antibody solution together with m3, m2 and MAP2 (1:1000, chicken) antibodies, following the same multi-labeling immunolabeling protocol

ARTICLE IN PRESS

ARTICLE IN PRESS

together used for the test samples (see above). Preincubation of the antibody with the recombinant protein resulted in a qualitative reduction of immunofluorescence intensity compared to controls (Supplementary Fig. 1O). However, the signal was not completely abolished. This partial blocking may reflect differences in epitope accessibility between the linearized peptide used for immunization and the folded recombinant protein, or kinetic limitations in the competition assay. Consequently, while the laminar distribution observed here matches established m1 receptor patterns, we interpreted relative intensity patterns rather than absolute protein quantification.

Cell density estimates of m1 and m3 protein and mRNA expressing neurons. As described in our previous work[41], we quantified the density of somata labeled for m1 and m3 protein and mRNA. Confocal image stacks from fields in L2-3 and L5-6 of ACC area 24 and LPFC ventral A46 (n = 2 fields per layer/area/case) were obtained using laser-scanning confocal microscope (Olympus FV3000). Image stacks were acquired using a 40x/1.4 NA oil immersion objective (Olympus UPlanXAPo) at a voxel resolution of 0.124µm x 0.124µm x 0.5µm. For each area, we identified 1-2 columns per section, and systematically imaged ROIs within L2-3 and L5-L6. We focused on imaging these layers where somata of pyramidal neurons mainly reside, since our goal is to validate expression patterns in ExNs in the snRNA-seq dataset (Barbas and Pandya, 1989). The resulting images were deconvolved to improve the signal-to-noise ratio and converted to 8-bit image files for analysis using cellSens software (Olympus). For each deconvolved image stack, we used semi-automated classifier tools in QuPath[189] to quantify the distribution of m1 and m3 cells co-expressing protein and mRNA as described[40]. For each field, the maximum z-projection of three 2-µm substacks of top, middle, and bottom optical slices were generated in Fiji/ImageJ (https://imagej.net/Fiji; RRID:SCR_002285) and imported into QuPath. Cell detection function was used to automatically segment somata of m1 protein^{+} cells as individual objects. The

ARTICLE IN PRESS

ARTICLE IN PRESS

segmented objects were checked for positive expression of neuronal MAP2 to include neurons (and exclude glia). Majority of the strongly labeled MAP2 neurons are excitatory, but lightly labeled non-pyramidal neurons were also included and are likely InN. The segmented objects were then classified based on their expression of m1 mRNA, m3 mRNA, and m3 protein using the semi-automated classifier tools in QuPath. The classifiers were based on a user-defined intensity threshold and was kept consistent within each case. The proportions of m1 and m3 mRNA and protein-expressing neurons were calculated by dividing each classified marker by the total number of detections (m1 protein$^+$ or m3 mRNA$^+$ and protein$^+$ cells).

Functional assessments of muscarinic receptor activation on spontaneous excitatory (EPSCs) and inhibitory (IPSCs) postsynaptic currents in layer 3 pyramidal neurons. In parallel to tissue preparation for biochemical experiments, a part of the fresh tissue blocks harvested from the ACC and LPFC were sectioned into 300-μm coronal slices in ice cold Ringer's solution or the NMDG recovery solution[190] (for cases PJG, PJJ and PJM, in mM: 92 NMDG, 2.5 KCl, 1.2 NaH_2PO_4, 26 $NaHCO_3$, 20 HEPES, 25 glucose, 2 thiourea, 5 sodium ascorbate, 3 sodium pyruvate, 0.5 $CaCl_2 \cdot 2H_2O$, and 10 $MgSO_4 \cdot 7H_2O$; pH 7.4) using a vibrating microtome (Leica VT1000S), as described[27]. The resulting slices were then placed into room temperature, oxygenated Ringer's and allowed to equilibrate for 1 hour. Following the equilibration periods, individual slices were placed into a submersion-type recording chamber (Harvard Apparatus, Holliston, MA) and mounted onto the stages of Nikon E600 infrared-differential interference contrast (IR-DIC) microscopes (Micro Video Instruments). All experiments took place at room temperature in oxygenated Ringer's solution (at a rate of 2-2.5mL/min), which improve the viability and duration of recordings from monkey cortical slices.

ARTICLE IN PRESS

ARTICLE IN PRESS

Neurons from L3 in each slice were selected via visual guidance under IR-DIC. Standard tight-seal, whole-cell patch-clamp recordings with simultaneous biocytin filling were obtained from L3 neurons, as described[27]. Electrodes were fabricated on horizontal Flaming and Brown micropipette puller (Model P-87, Sutter Instruments, Novato, CA, USA) and were filled with potassium methanesulfonate-based internal solution (in mM: 122 KCH_3SO_3, 2 $MgCl_2$, 5 EGTA, 10 NaHEPES, with 1% biocytin, pH 7.4) with resistances of 3-6 MΩ in the external Ringer's solution. Data were acquired using EPC-9 or EPC-10 patch-clamp amplifiers with the PatchMaster software (HEKA Elektronik, Lambrecht, Germany). The series resistance ranged from 10 to 15 MΩ and was not compensated. Series and access resistance were monitored frequently, and if there was a change of >10%, the cell was discarded. Bessel filter frequency was 10 kHz and sampling frequency was at 7 kHz for voltage-clamp recordings and 12 kHz for current-clamp recordings.

Neurons were included in electrophysiological analysis if they had a resting membrane potential of ≤ -55mV, stable access resistance, an action potential (AP) overshoot, and repetitive firing responses, as described[179]. Spontaneous excitatory and inhibitory synaptic currents (EPSCs and IPSCs) were recorded for at least 2 minutes at a holding potential of -80mV and -40mV, respectively[27] followed by a continuous bath application of a non-specific ACh agonist carbachol (CCH, 10μM) and recording of EPSCs (after 6-8 minutes of CCH) and IPSCs (after 10mins of CCH). Analysis of synaptic events was performed using MiniAnalysis (Synaptosoft, Decatur, GA, USA), with the event detection threshold set at maximum root mean squared noise level (5 pA) as described previously. We examined the frequency, mean amplitude, area under the curve and kinetics (rise and decay time, and half-width). Drug-treated cells were classified into "increase", "decrease" or "no change" subgroups in response to CCH. Classification as a responder (either increase or decrease) required satisfying two conditions: (1) a statistically significant shift in the

ARTICLE IN PRESS

ARTICLE IN PRESS

inter-event interval (IEI) cumulative probability distribution (Kolmogorov-Smirnov, K-S test) or significant differences (repeated measures ANOVA) between the time histograms (number of events over time) before and after CCH; (2) a change in mean frequency exceeding ±20% of baseline.

In a subset of cells, after the 10 min CCH bath exposure, EPSCs and IPSCs were subsequently recorded after a 15 min washout in Ringer's solution. We identified 3 classes of cells based on significant differences across the three treatment conditions: 1) cells that exhibited a "transient CCH effect", with a significant CCH effect followed by a washout return to baseline effect (K-S test, $p < 0.05$ for CTR v CCH and CCH v washout; CTR = washout), 2) cells that exhibited a "sustained CCH effect", with a CCH effect but no washout effect ($p < 0.05$ for CTR v CCH and CTR v washout, CCH = washout) and 3) cells that exhibited a "delayed CCH effect", with no CCH effect, but washout was significantly different from baseline ($p < 0.05$ for CTR v washout and CCH v washout; CTR = CCH). Further as another internal control for time-dependent effect, we ran some rundown experiments in a subset of cells (n = 2 ACC, 1 LPFC each from two cases), in which cells are recorded in Ringer's ("vehicle") for the same amount of time as CCH exposure, and found no significant changes in EPSC/IPSCs across the course of recording (Supplementary Fig. 4G).

Processing of filled neurons for assessments of spine density. During whole-cell patch-clamp recordings, neurons were filled with biocytin (0.5%, Millipore Sigma) and processed for post-hoc morphological assessments, as described in our previous work[27,191]. To visualize recorded cells filled with biocytin, 300-µm slices were fixed in 4% paraformaldehyde in 0.1 M phosphate-buffered saline (PBS; pH = 7.4), incubated for 2 h in 1% Triton X (in 0.1 M PBS), followed by 48 h in streptavidin-Alexa Fluor 488 or 750 (diluted 1:500 in 0.1 M PBS; Invitrogen). Slices were

ARTICLE IN PRESS

washed in 0.1M PB, mounted on glass slides, and coverslipped with Prolong Gold mounting media (ThermoFisher).

Confocal imaging and spine analyses of filled neurons. A subset of neurons recorded with complete filling of somata, apical and basal dendrites (with no cut branches in the proximal third) were included in morphological analyses. Image stacks were acquired using an Olympus FV3000 confocal laser-scanning microscope (Evident/Olympus Inc). For assessment of filled spines, a series of image stacks were acquired (at 0.04 x 0.04 x 0.3 µm per voxel, using 60x/1.5 NA oil-immersion objective, UPlanXApo, Evident/Olympus Inc) with a 488 nm or 750 nm excitation laser. For each neuron, confocal stacks within 100 µm from the tissue surface were acquired to image one complete basilar dendritic branch, and the main apical trunk followed to the end of one complete distal apical dendritic branch. Image stacks are then deconvolved using AutoQuant (Media Cybernetics, Bethesda, MD, USA) or Cellsens (Evident/Olympus Inc), and tiled and analyzed using Neurolucida 360 (MBF Bioscience; RRID:nif-0000-10294) [27].

Subsampled basal and apical dendrites were manually traced and spines along these dendrites were manually marked and classified by subtypes and size, as described previously [191]. Spines were classified based on head width and neck length as follows: thin (width > 0.6 µm), mushroom (width ≥ 0.6 µm), stubby (lacking a neck), filopodia (neck length ≥ 0.3µm), and other (branched spines or those that cannot be identified). The following parameters were compared across cells in slices that were treated with control Ringer's, 10 min of 10 µM CCH, or CCH followed by 15 min of washout in Ringer's: 1) spine densities (number of spines per micron of dendritic length); 2) proportion of spines by subtype; 3) length of spine necks and diameters of spine heads in apical and basal dendrites.

ARTICLE IN PRESS

ARTICLE IN PRESS

Statistics and Reproducibility. All analyses of transcriptomic snRNAseq data were employed using packages in R software (RRID:SCR_001905) and functional annotation analyses from DEGs were employed with EnrichR (https://maayanlab.cloud/Enrichr/; RRID:SCR_001575)[55]. All analyses for electrophysiological and spine data were conducted blinded to area and drug treatment. All statistical tests were conducted in MATLAB (v R2023a; RRID:SCR_001622). The number, age and sex of subjects for each experiment are summarized in Supplementary Table 1, and transcriptomic analyses, statistical analyses and raw datasets are presented in Supplementary Data 1-9. Comparisons of population distributions were done using a Fisher's exact test or Kolmogorov-Smirnov (K-S) test. For all analyses, parameters were first tested for normality using a K-S test, and significance level of $p < 0.05$ was used.

For the snRNAseq dataset (n=4 males, ages = 8.5-24.8 y), DEGs across isolated nuclei were compared between cell populations and areas (as described above). Post-analysis filtering of DEGs was used to cutoff at an adjusted p-value of $p < 0.05$ and a $|Log2FC| > 0.25$ (Supplementary Data 1-4). Inter-subject variability by age was also assessed for our relevant markers. For IHC/HCR-FISH data (n = 2 males and 2 females, aged 8.4-8.9 y; Source data for graphs in Supplementary Data 7), statistical comparisons between markers (m1 vs m3 protein/mRNA), within each area and layer were employed using a paired t-test with Welch's correction. For electrophysiology and spine analyses (Source data for graphs in Supplementary Data 8 and 9), we compared cells recorded and filled from n = 6 males and n = 3 females adult monkeys (ages = 7.5-16.8 y). For electrophysiological data, recordings were obtained from L3 pyramidal neurons of ACC (n=20 EPSC from 9 cases, and n=16 IPSC from 7 cases) and LPFC (n=14 EPSC and n=10 IPSC from 7 cases) before and after a 6-8 min bath exposure to CCH (10µM; Supplementary Fig. 4A, B). In a subset of cells (n = 6 ACC cells from 4 cases; and n = 3 LPFC cells from 2 cases),

ARTICLE IN PRESS

EPSCs and IPSCs were recorded before and after 10 min of CCH bath exposure, and after a 15 min washout in Ringer's solution. The washout synaptic responses were too stochastic/heterogenous to run comparisons of average responses across many cells. Instead, we have statistically compared within individual cells the number of events and IEI at baseline control (CTR), CCH and washout conditions, using a repeated measures design (Supplementary Data 5; Supplementary Fig. 4). For spine analyses, we analyzed cells from slices treated with control Ringer's solution (n = 15 ACC and n = 9 LPFC cells from 7 cases), 8 mins of 10 µM CCH (n = 5 ACC cells from 2 cases, n = 4 LPFC cells from 3 cases), or 10 mins of CCH followed by 15 min of washout in Ringer's (n = 3 ACC cells, n = 6 LPFC cells from 2 cases). We obtained a sufficient number of cells per group to compare between 2 areas (ACC v LPFC) and between 3 drug treatment conditions (CTR vs CCH vs washout) using a Two-Way ANOVA with Fisher's LSD post-hoc test (Supplementary Data 6). Due to the limited sample size of cells per area and drug treatment group, we could not perform comparisons between-sexes. Further, our snRNA-seq data is consist only of tissue from male monkeys. Thus, our study is limited in examining the effects of sex across our outcome measures.

ARTICLE IN PRESS

Figure Legends

Figure 1. Predominant neuronal expression and nuclear retention of *CHRM3* in ACC and LPFC.
(**A**) Photographs of the rhesus monkey brain showing locations of ACC (area 24) and LPFC (area 46) regions of interest and schematic of experimental workflow. Brain images and FACS plot are from original data; other schematic images were created in BioRender (https://BioRender.com/uixnhif). (**B**) UMAP plot based on snRNA-seq showing transcriptomically distinct clusters corresponding to major cell types in ACC and LPFC (see Supplementary Fig. 1). (**C**) Violin plots showing expression level of *CHRM1, CHRM2, CHRM3, CHRM4* within each major cell type in ACC vs. LPFC. (**D**) UMAP feature plots showing expression pattern of the *CHRM1-4* in ACC and LPFC; (**E**) Stacked horizontal bar graph showing percentage of total nuclei in ACC and LPFC expressing *CHRM1, CHRM2, CHRM3, CHRM4*. (**F**) Proportion of nuclei expressing *CHRM1-4* out of total nuclei by cell type for each area. (**G**) Representative z-maximum projection confocal images (5 optical stacks) from ACC and LPFC

ARTICLE IN PRESS

L2-3 showing the cellular/ subcellular distribution of m1 protein (green) and mRNA (magenta) and m3 protein (cyan) and mRNA (red). Note the predominantly cytoplasmic localization of *CHRM1*, versus the diffused distribution of *CHRM3* within nuclear and cytoplasmic compartments. (**H**) Density of total cells immuno-labelled for m1+ (green) and m3+ (cyan) proteins in ACC and LPFC (n=4 monkeys). In L2-3 of ACC, there was a significantly greater density of m1+protein neurons in L2-3 compared to m3+protein cells (Welch t-test **$p < 0.001$ in ACC; and a trend $^{\#}p = 0.07$ in LPFC). (**I**) Violin plots of mean intensity within individual cells expressing m1 and m3 protein (left) and mRNA (right). Intensity of m1+protein label is significantly greater than m3+protein label in both areas (***$p < 0.001$; ACC: n = 3013 cells, and LPFC: n = 3344 cells, from 4 monkeys). (**J**) Proportion of total m1+ and total m3+ mRNA and protein expressing cells in ACC and LPFC. Open bars show the proportion of cells that are mRNA negative but protein positive (mRNA-/PROT+), and filled bars show the proportion positive for mRNA with (mRNA+/PROT+, dark gray) or without (mRNA+/PROT-, cyan) protein. Note the presence of m3+ cells expressing mRNA but no protein (mRNA+/PROT-, cyan). (**K**) Scatter plot of mRNA/protein label intensity within individual cells and linear regression analyses in ACC and LPFC, showing correlations of m1 and m3 mRNA vs protein. (**L**) Proportion of cells showing mRNA label localized only in the cytoplasm, or within nuclei and cytoplasm. Nuclear vs cytoplastic localization was based on the central versus peripheral localization of label and its overlap with MAP2 cytoplasmic labeling.

Figure 2. *CHRM1-3* show distinct distribution across layer-specific ExNs and neurochemical InN subclasses in ACC and LPFC.
(**A**) Dot plot showing expression level of the top region-specific enriched genes in ACC vs LPFC ExNs. (**B**) Top enriched Gene-Ontology (GO) Biological Processes terms associated with the region-specific genes generated using EnrichR[55]. (**C**) Pie chart showing the overall proportion of ExN expressing/co-expressing specific *CHRMs* in ACC and LPFC. Inset shows UMAP highlighting the population of ExNs (green) together with other cell types. (**D**) UMAP plot (left) after re-clustering of ExNs annotated based on layer-specific subpopulations identified via expression of layer-specific genes in each cluster shown in dot plot (right; see Supplementary Fig. 2 and Supplementary Table 2). (**E**) Pie chart showing the overall proportion of InN expressing/co-expressing *CHRMs* in ACC and LPFC. Inset shows UMAP highlighting the population of InNs (blue) together with other cell types. (**F**) UMAP plot (left) after re-clustering of InNs showing 7 distinct clusters/subpopulations annotated based on expression of neurochemical markers. Dot plot shows expression pattern of a subset of markers for distinct neurochemical subclasses of InNs based on the literature (see Supplementary Fig. 2). (**G**) Feature UMAP plots showing the expression pattern of *CHRM1-4* following the re-clustering of ExNs and (**H**) InNs. (**I**) Within each ExN laminar subpopulations (left) and InN subtypes (right): proportion of cells with single, coexpression (>1) or no expression of *CHRM1-4* are presented as a stacked bar plot, UL=upper layers, DL=deep layers. (**J**) Within ExNs laminar subpopulations (left) and InN subtypes (right) with *CHRM1-4* coexpression: proportion of cells with specific combinations of *CHRM1-4* coexpression are presented as a stacked bar plot.

Figure 3. *CHRM* enrichment define cell-specific transcriptomic signatures aligning with mAChR functional classes.
(**A**) Bar graph of the number of DEGs in total, ExN or InN enriched in *CHRM1* relative to *CHRM2* (light blue); enriched in *CHRM3* relative to *CHRM2* (dark blue); and enriched in *CHRM1* relative

ARTICLE IN PRESS

to *CHRM3* (purple). (**B**) Top significantly enriched KEGG pathway (top bars) and GO biological processes (bottom bars) terms generated based on DEGs between *CHRM1+* relative to *CHRM2+* ExNs (light blue) and (**C**) *CHRM3+* relative to *CHRM2+* ExNs (dark blue). The data was generated using EnrichR[55] and significance enrichment was defined as p-value<0.05, Benjamini. (**D-F**) Fold-change of top *CHRM1* vs. *CHRM2* and *CHRM3* vs. *CHRM2* DEGs within ACC and LPFC ExNs, related to: (**D**) KEGG term "Glutamatergic Synapse" and GO term "Chemical Synaptic Transmission" (teal text in panels B and C); (**E**) KEGG term "Calcium Signaling", and GO term "Calcium transmembrane import into the cytosol" (purple text in panels B and C)' and (**F**) KEGG term "Axon Guidance", and GO term "Nervous System Development" (pink text in panels B and C). (**G**) KEGG pathway and GO terms from *DEGs* between *CHRM3+* relative to *CHRM2+* InNs (dark blue), *CHRM1+* relative to *CHRM2+* InNs (light blue), and *CHRM1+* relative to *CHRM3+* InNs (purple). (**H-J**) Fold-change of top *CHRM1* vs. *CHRM2, CHRM3* vs. *CHRM2,* and *CHRM1* vs. *CHRM3* DEGs within ACC and LPFC InNs, related to: (**H**) KEGG/GO term "Ca Signaling" and "Ca Ion Transport", and KEGG term "Cholinergic Synapse" (purple text in panel G); (**I**) Plasticity related terms – GO terms "Nervous system development" and "Regulation of Growth Factor Stimulation" (pink text in panel G); (**J**) GO term "Chemical Synaptic Transmission" (teal text in panel G);. See Supplementary Data 2 and 3 for a full list of DEGs and enriched terms, and Supplementary Fig. 3 for volcano plots.

Figure 4. Regional differences in plasticity-related transcriptomic signatures within *CHRM1-3* enriched neurons. (**A**) Bar graph of the number of DEGs enriched in ACC relative to LPFC, within *CHRM1-4+* expressing neurons (total, ExNs, and InNs). (**B, C**) Volcano plots of the DEGs between ACC and LPFC, within *CHRM1-3+* InNs (**B**) and ExNs (**C**). (**D-F**) Top significantly enriched KEGG pathway (top bars) and GO biological processes (bottom bars) terms generated based on DEGs between ACC relative to LPFC for: (**D**) *CHRM1+ ExNs* (light blue). Inset (d) shows fold-change of top ACC vs. LPFC DEGs related to: "Rap1 Signaling" and "Long Term Potentiation"; (**E**) *CHRM2+ ExNs* (orange). Insets (e1, e2) show fold-change of top ACC vs. LPFC DEGs related to "Long Term Depression" (LTD), "Calcium Signaling" (Ca), and "Regulation of Sodium Ion Transport" (Na); and (**F**) *CHRM3+* ExNs (dark blue). Inset (f) shows fold-change of top ACC vs. LPFC DEGs related to "GABAergic Synapse" (GABA) and "Glutamatergic Synapse" (GLU). (**G-I**) Fold-change of top ACC vs. LPFC DEGs within *CHRM1* and *CHRM3* ExNs, related to the following common terms (in bold black text in D, F): (**G**) "Cell-Cell Adhesion via Plasma Membrane Adhesion Molecules" (Adhesion); (**H**) "Axon Guidance"; and (**I**) "Chemical Synaptic Transmission". (**J**) Top significantly enriched GO biological processes terms generated based on DEGs between ACC relative to LPFC in *CHRM3+* InNs (dark blue). Inset (j) shows fold-change of top ACC vs. LPFC DEGs related to "Anterograde Trans-Synaptic Signaling" and "Homophilic Cell Adhesion Via Plasma Membrane" (Adhesion). The data was generated using EnrichR[55] and significance enrichment was defined as p-value<0.05, Benjamini. See Supplementary Data 4 for a full list of enriched terms and DEGs.

Figure 5. Cholinergic agonist amplified regional differences in excitatory:inhibitory synaptic tone of ACC vs. LPFC pyramidal neurons. (**A , B**) Representative traces of (**A**) spontaneous EPSCs (Vhold at -80mV) in ACC (n=20 cells from 9 cases) and LPFC LPFC (n=14 from 7 cases),; and (**B**) spontaneous IPSCs (Vhold – 40mV) in ACC (n=16 cells from 7 cases) and LPFC (n=10 from 7 cases) L3 pyramidal neurons, before and after bath application of 10 µM carbachol (CCH). (**C**) Schematic of whole cell patch clamp recordings from L3 pyramidal neurons (left) and

ARTICLE IN PRESS

ARTICLE IN PRESS

experimental design for studying synaptic currents (right). (**D, E**) Time-course of number of EPSC and IPSC events (mean per 10 sec time bin) in ACC and LPFC neurons before (control) and during the last 8-10 min (D, EPSCs) and 10-12 min (E, IPSCs) of bath application of 10µM CCH. Error bars = SEM for each bin. (**F**) Cumulative distribution histograms of inter-event-intervals (IEI) of EPSCs and IPSCs from representative cells that exhibited significant CCH+ effects. (**G**) The proportion of ACC or LPFC neurons that had a decrease, increase, or no change in the frequency of EPSCs after CCH. (**H**) Box and whisker plots of EPSC properties (frequency, amplitude, decay time) in neurons that exhibited a decrease in EPSC events before and after 6-8 min in CCH. ** $p \leq 0.01$. (**I**) The proportion of ACC and LPFC neurons that had a decrease, increase, or no change in the frequency of IPSCs after CCH. (**J**) Box and whisker plots of IPSC properties [frequency, amplitude, and total charge (frequency x area)] before and after 10 min in CCH. (**K**) The estimated E:I ratio based on the frequency and mean area of each neuron. (**L**) Scatter plots of excitatory versus inhibitory total charge in each ACC (*left*) and LPFC (*right*) neuron before (open circles) and after CCH (filled circles). The dotted line in both plots represent the linear relationship whereby E=I. In majority of ACC neurons, IPSC total charge dominates, especially after CCH. In LPFC neurons, EPSC total charge dominates. *$p \leq 0.05$, ** $p \leq 0.01$, *** $p \leq 0.001$(see Supplementary Data 5). Supplementary Fig. 4 shows washout control experiments.

Figure 6. Cholinergic agonist promoted motile post-synaptic spine morphologies in ACC and LPFC pyramidal neurons. (**A**) Box-and-whisker and vertical scatter plots of spine density (total and by subtype) on apical and basal dendrites of individual ACC and LPFC L3 pyramidal neurons in slices treated with control Ringer's (n = 15 ACC, 9 LPFC cells from 7 cases), 10 mins of 10 µM CCH (n = 5 ACC from 2 cases, 4 LPFC from 3 cases), and 10 mins of 10 µM CCH followed by 15 min of washout in Ringer's (n = 3 ACC, 6 LPFC from 2 cases). (**B**) Representative z-maximum projections of confocal images of mid-apical dendrites of control and CCH treated ACC and LPFC L3 pyramidal neurons. The neurons were filled with biocytin and labeled with Streptavidin-Alexa 488. (**C**) Average proportion of spines per subtype on apical and basal dendrites of control (CTR), CCH and CCH+Washout (W) treated L3 pyramidal neurons in ACC and LPFC, as represented by stacked bar graphs (Fisher's exact test, $p < 0.0001$). (**D**) Box and whisker and vertical scatter plots of the average major diameter of spine subtypes on control, CCH and CCH+Washout treated pyramidal neurons. *$p \leq 0.05$, ** $p \leq 0.01$, *** $p \leq 0.001$. (see Supplementary Data 6). (**E**) Summary schematic of findings showing cell-specific *CHRM1/3+* vs *CHRM2+* ExNs and InNs enrichment patterns, associated potential differences in mRNA-protein dynamics and trafficking of m1 vs m3 (1), and regional differences in downstream functional effects of ACh on synaptic plasticity and function, within the context of known laminar and regional differences in excitatory and inhibitory connectivity, cellular composition (2) and mAChR subcellular localization (3, 4), based on current data and previous studies[40,41].

ARTICLE IN PRESS

ARTICLE IN PRESS

Editorial Summary:

Integrated transcriptomic, histological, and functional profiling in macaques reveals how muscarinic receptors differentially regulate synaptic plasticity and excitation-inhibition balance in the anterior cingulate versus lateral prefrontal cortex.

Peer Review Information:

Communications Biology thanks William Howe and the other, anonymous, reviewer(s) for their contribution to the peer review of this work. Primary Handling Editor: Benjamin Bessieres.

ARTICLE IN PRESS

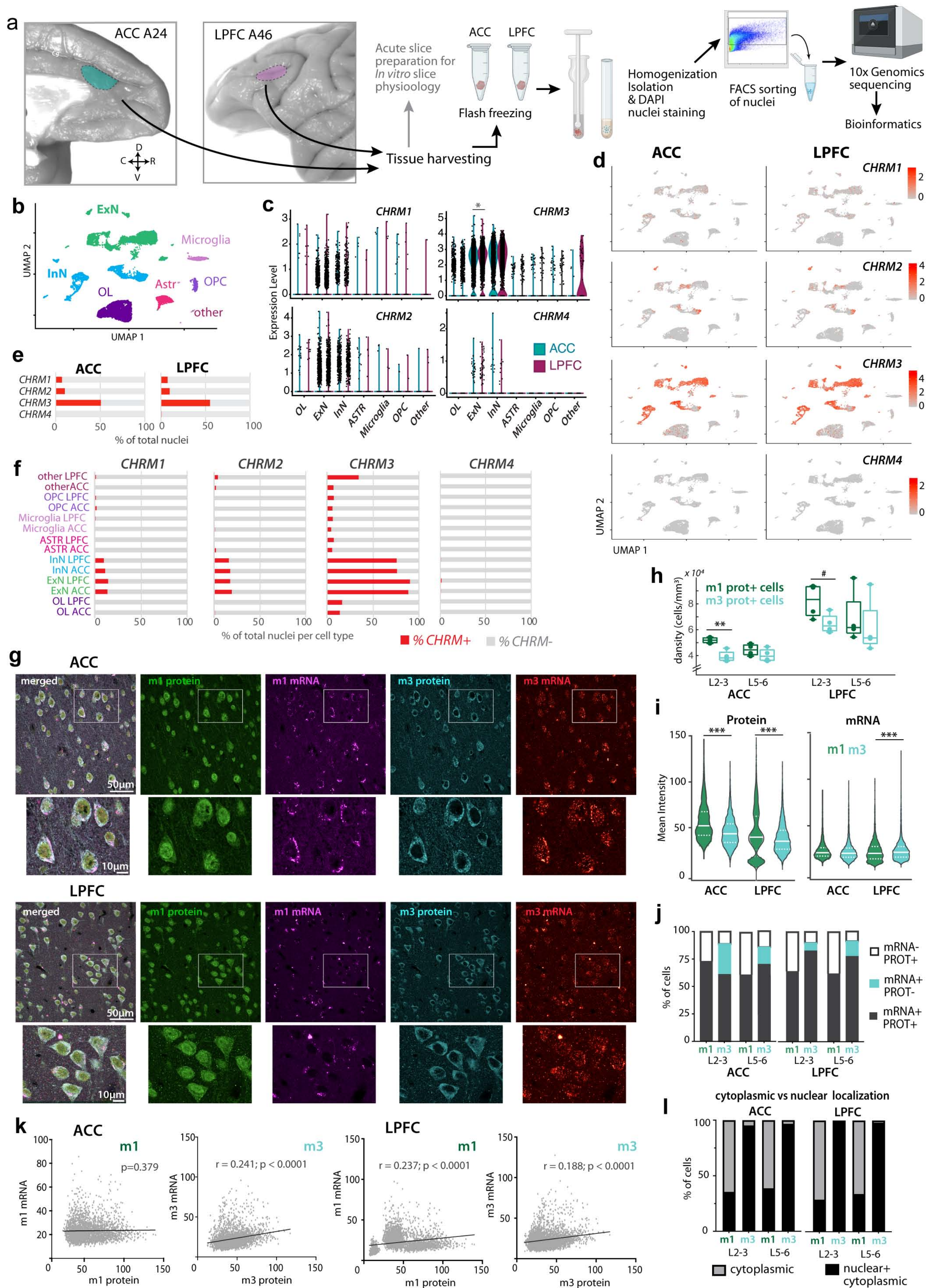

a
ACC A24
LPFC A46
Acute slice preparation for In vitro slice physiology
ACC
LPFC
Flash freezing
Tissue harvesting
Homogenization Isolation & DAPI nuclei staining
FACS sorting of nuclei
10x Genomics sequencing
Bioinformatics
b
ExN
Microglia
InN
Astr
OPC
OL
other
UMAP 1
UMAP 2
c
CHRM1
CHRM2
CHRM3
CHRM4
Expression Level
ACC
LPFC
OL
ExN
InN
ASTR
Microglia
OPC
Other
d
ACC
LPFC
UMAP 1
UMAP 2
e
ACC
LPFC
% of total nuclei
f
other LPFC
otherACC
OPC LPFC
OPC ACC
Microglia LPFC
Microglia ACC
ASTR LPFC
ASTR ACC
InN LPFC
InN ACC
ExN LPFC
ExN ACC
OL LPFC
OL ACC
% of total nuclei per cell type
% CHRM+
% CHRM-
g
ACC
LPFC
merged
m1 protein
m1 mRNA
m3 protein
m3 mRNA
50μm
10μm
h
m1 prot+ cells
m3 prot+ cells
dansity (cells/mm³)
x 10⁴
L2-3
L5-6
ACC
LPFC
i
Protein
mRNA
m1 m3
Mean Intensity
ACC
LPFC
j
% of cells
mRNA-PROT+
mRNA+PROT-
mRNA+PROT+
m1 m3
L2-3
L5-6
ACC
LPFC
k
ACC
LPFC
m1
m3
p=0.379
r = 0.241; p < 0.0001
r = 0.237; p < 0.0001
r = 0.188; p < 0.0001
m1 mRNA
m3 mRNA
m1 protein
m3 protein
l
cytoplasmic vs nuclear localization
ACC
LPFC
% of cells
cytoplasmic
nuclear+ cytoplasmic

ARTICLE IN PRESS

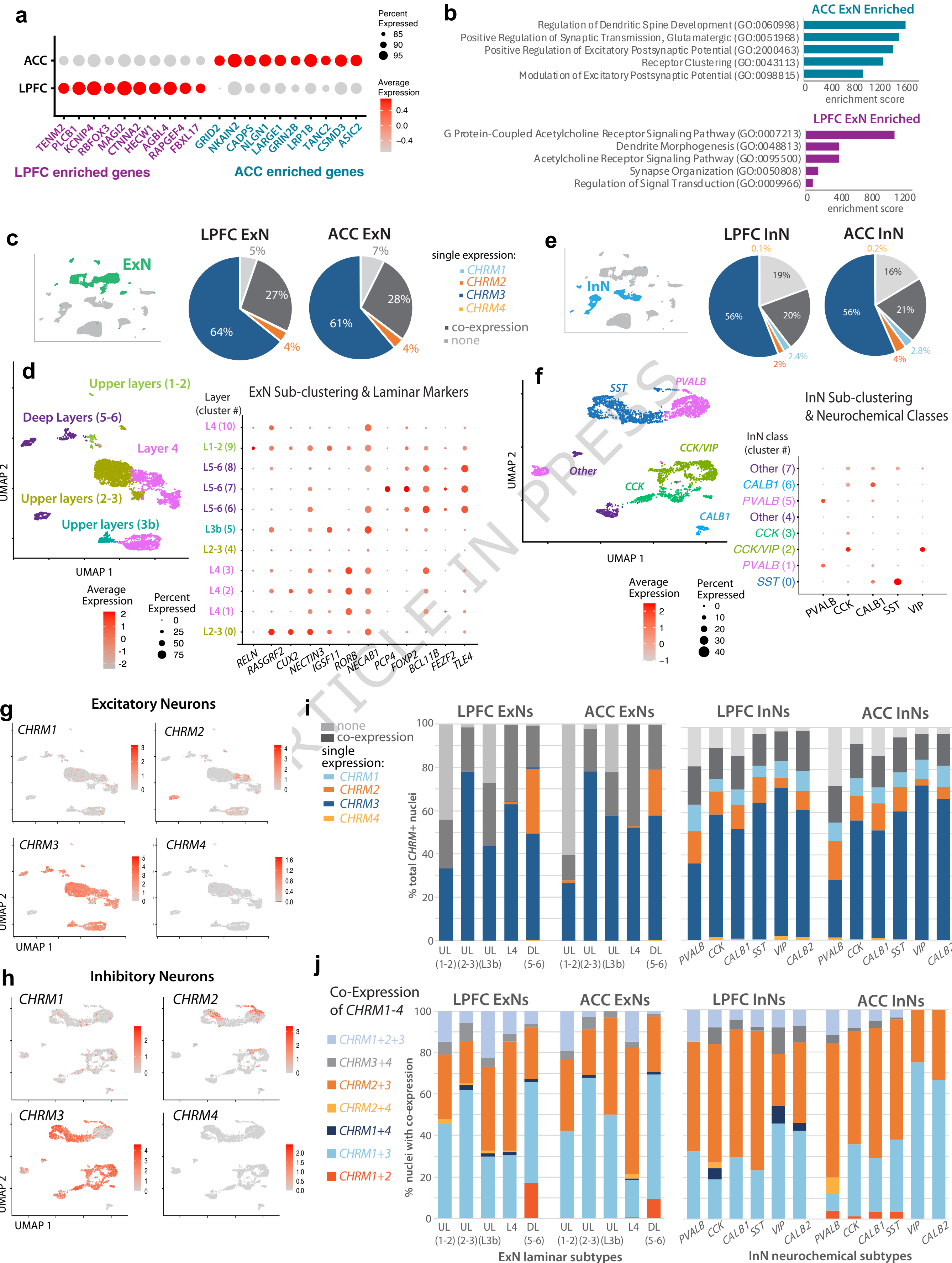

ARTICLE IN PRESS

ARTICLE IN PRESS

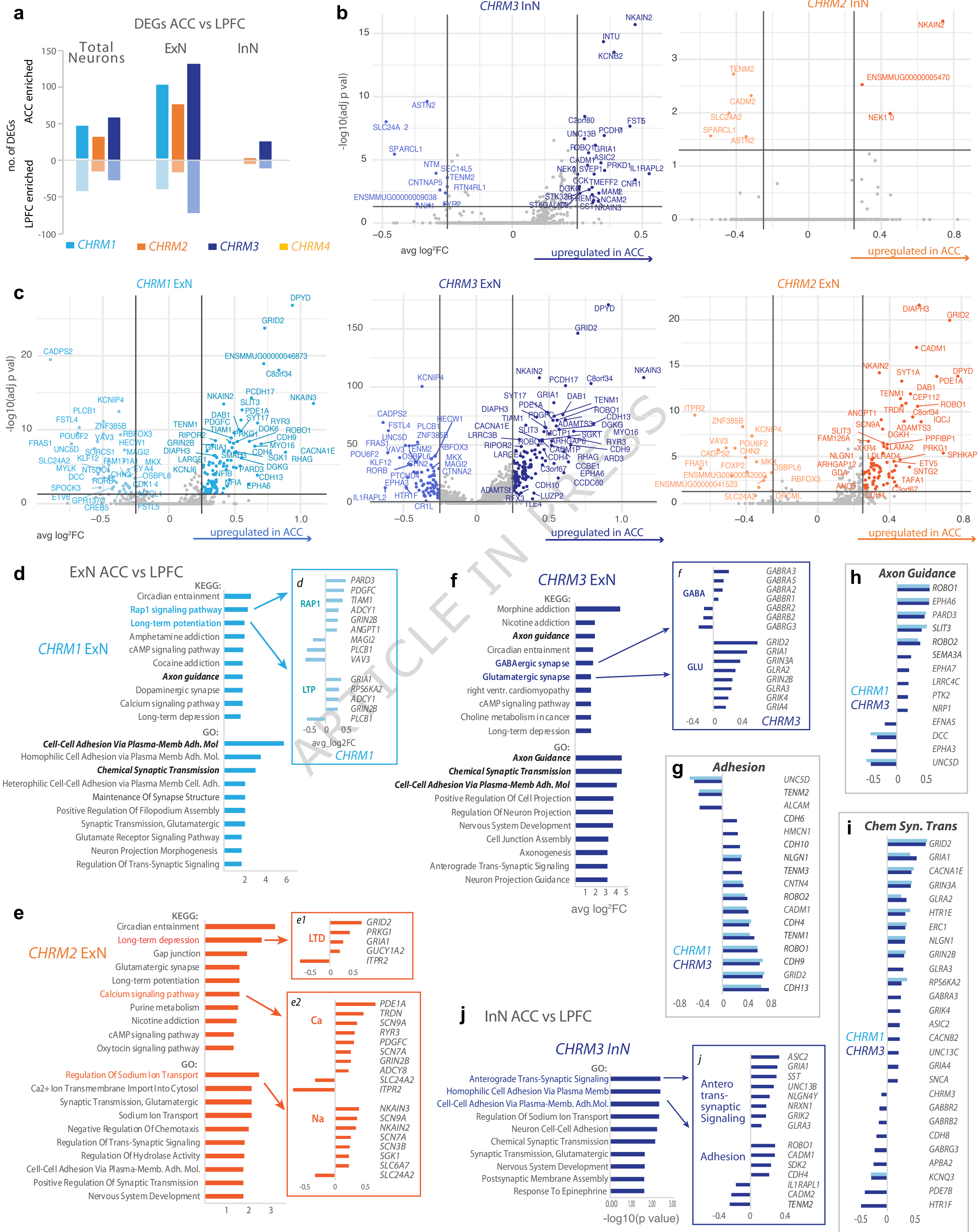

ARTICLE IN PRESS

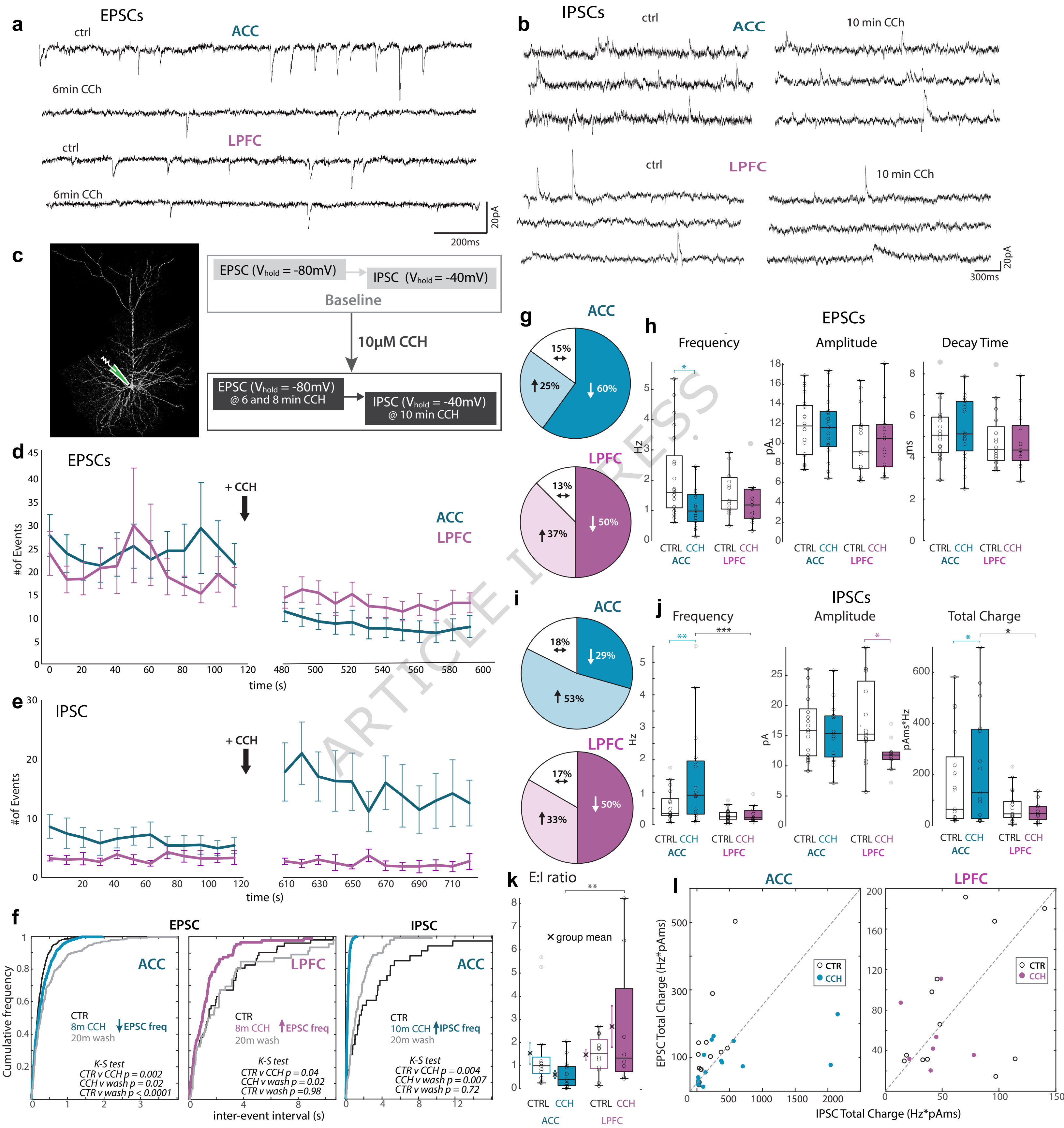

ARTICLE IN PRESS

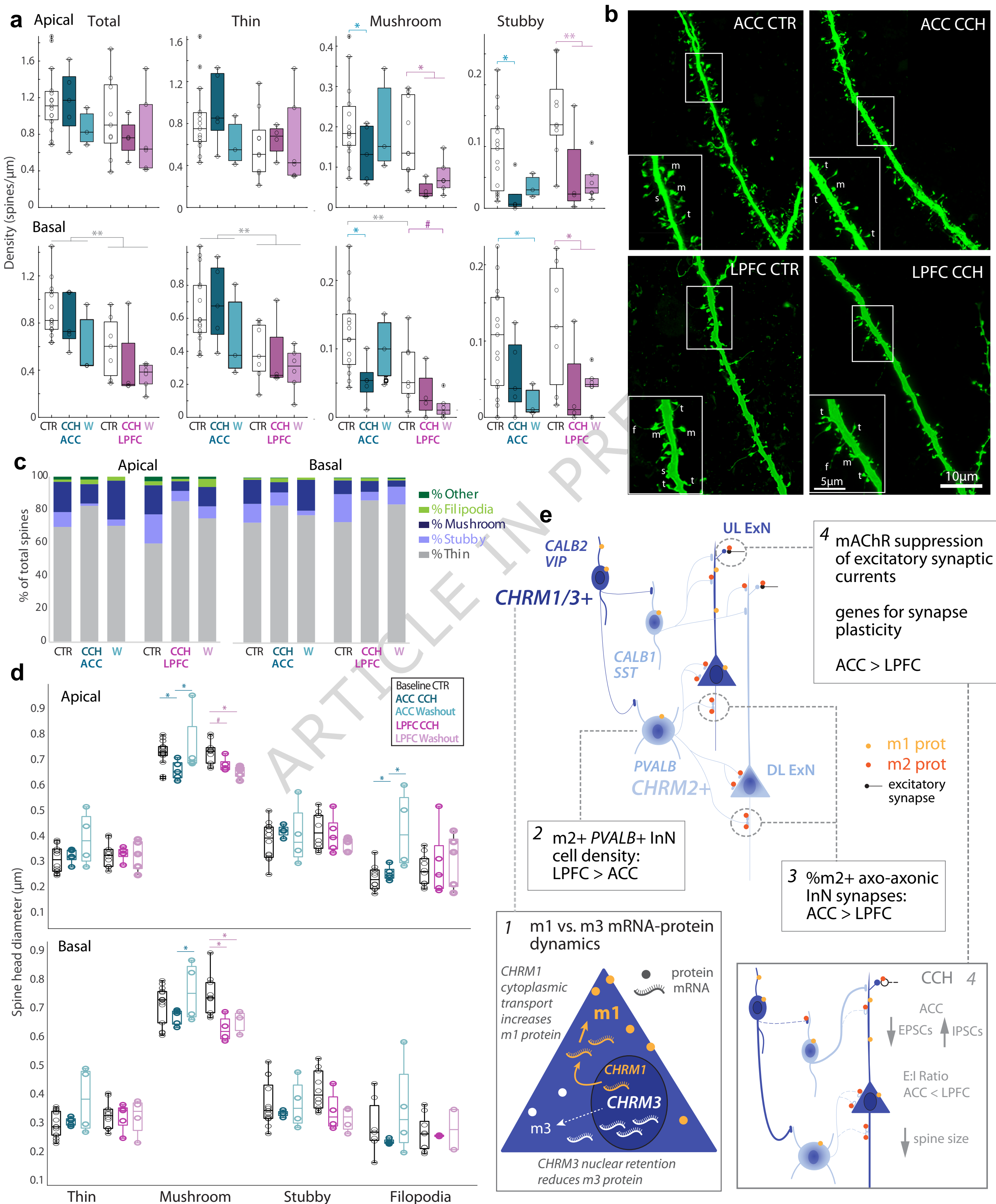

ARTICLE IN PRESS